9-1-1987

The Fabrication, Testing and Simulation of Germanium Thermophotovoltaic Cells

Daniel L. C. Huang
Purdue University

M. S. Worley
Purdue University

J. L. Gray
Purdue University

R. J. Schwartz
Purdue University

Final Report for NRL Contract N00173-79-C-0362

**The Fabrication, Testing and Simulation
of Germanium Thermophotovoltaic Cells**

by

Daniel L. C. Huang
M. S. Worley
J. L. Gray
R. J. Schwartz

School of Electrical Engineering
Purdue University
West Lafayette, IN 47907

Submitted to the
Naval Research Laboratories

September 1987

TR-EE 87-34

Table of Contents

CHAPTER 1

INTRODUCTORY COMMENTS

1.1 Introduction

This is the final report on NRL Contract N00173-79-C-0362. The purpose of this investigation was to fabricate germanium photovoltaic cells and to examine the feasibility of using them in a thermophotovoltaic system for the generation of electrical power in space. The energy source was to be solar. Systems aspects of the collection of solar energy and rejection of waste heat were not a part of this study.

The strategy employed in this investigation was the following.

1. Fabricate germanium photodiodes.
2. Carefully characterize these photodiodes.
3. Simulate the performance of these photodiodes using a detailed numerical model of the cell and the illuminating spectra.
4. Use this simulation program to project the potential performance of germanium photodiodes in a thermophotovoltaic system under various assumptions about future improvements in diode performance and under various thermophotovoltaic spectral conditions.

1.2 Primary Problems Encountered in the Investigation

Processing technology for germanium semiconductor devices has made little progress in the last 20 years. During the course of this investigation, many of the developments which have proven so effective in silicon device fabrication were applied to germanium, i.e., pyrolytic deposition of insulators and masks, ion implantation, thermal annealing, and oxide surface passivation. Since little of this technology was widely used for germanium at the beginning of this study, nearly every step of the fabrication process involved a development effort.

No detailed numerical analysis program existed for germanium devices at the start of the project. This necessitated modification of a silicon device model (SCAP1D). Modifications included development of: a suitable intrinsic band gap model; models for heavy doping effects; a model of mobility dependence on doping; a model for the intrinsic carrier concentration; a model for optical absorption in intrinsic and doped germanium; models for blackbody radiation and filtered radiation to simulate multiple cell systems; models to handle ion implantation and the doping dependence of lifetime.

1.3 Report Organization

In this report, Chapter 2 is devoted to a discussion of the modification of SCAP1D. Chapter 3 discusses the fabrication process used in this work. Chapter 4 is devoted to characterization of the cells which were fabricated. Chapter 5 discusses the results of using the modified one-dimensional germanium analysis code to model the experimental results of Chapter 4. Chapter 6 is devoted to the results of application of the computer model to the design of an optimized germanium cell, and to predictions of the performance of germanium cells under various assumptions about the illuminating spectra.

1.4 Summary of Results

1. High quality planar germanium photocells were fabricated with leakage currents lower than previously available devices.

2. Dark current-voltage, illuminated current-voltage and spectral response measurements were performed on the cells.

3. A numerical model which is capable of modeling the measured cell performance, as well as predicting future performance, was developed.

4. Presently available cells are limited by residual damage induced by ion implantation.

5. Improved cells will eventually be limited by the failure of the back surface field to contain minority carriers in the base of the cell.

6. TPV cells will be adversely affected by free carrier absorption in the base of the cell. This will require that a front surface (rather than a back surface) selective reflector be used.

7. An optimized cell design was developed.

8. Optimized cells used in conjunction with a high quality front surface selective reflector should be capable of conversion efficiences (cell) in excess of 30%.

9. Development of a highly efficient front surface selective reflector should receive high priority in any future work.

CHAPTER 2

CONVERSION OF SCAP1D TO GERMANIUM

2.1 Required Modifications

SCAP1D is a detailed numerical code which allows the analysis of silicon photovoltaic cells under a variety of operating conditions. SCAP1D has been used for a number of years to simulate the performance of silicon solar cells and to predict the effect of various design changes on the performance of these cells. In addition, it has provided a great deal of insight into the physics of the operation of such solar cells. One of the early tasks performed under this program was to modify SCAP1D to allow its use for germanium thermophotovoltaic (TPV) cells. The modifications required obvious changes in materials parameters and also included the addition of illuminating spectra which are unique to thermophotovoltaics.

2.1.1 Band gap

It was necessary to change the band gap from the a value appropriate for silicon to the value for germanium. The model contains information on the temperature dependence of the intrinsic band gap. This had to be modified to values appropriate to germanium. In addition, it has been shown that in silicon photovoltaic cells, heavy doping effects can dramatically influence the performance of the photovoltaic cell. While no experimental evidence is available, at this time, as to the effect of heavy doping on germanium photovoltaic cells, there is ample theoretical evidence that band gap narrowing will occur in germanium just as it does in silicon. Heavily doped regions are found in the emitter and the high-low junctions of a germanium thermophotovoltaic cell. Mahon has produced extensive theoretical calculations on the effects of heavy doping on both silicon and germanium,[1] Lanyon and Tufts [2] have produced a theory which is based on classical arguments and should apply to germanium as well as silicon and Landsberg[3] has presented still a third model which appears to apply to germanium. SCAP1D was modified to allow the use of any one of the three models, or no band gap narrowing at all, in the calculation of the performance of the germanium cells.

2.1.2 Mobility

As in the case of band gap narrowing, the subroutines which determine the dependence of carrier mobility on temperature and doping conditions needed to be modified to values appropriate to germanium. A Caughey-Thomas fit was used.

2.1.3 Intrinsic Carrier Concentration

The intrinsic carrier concentration is a function of band gap, temperature, and doping. Appropriate modifications were made to the subroutine which determines the intrinsic carrier concentration as a function of these parameters.

2.1.4 Optical Absorption Processes

The optical absorption coefficient is a function of temperature, frequency, and free carrier concentration. The subroutine in the code takes into account the appropriate band gap, the effects of free carrier absorption, and the effects of doping on the absorption coefficient. Thermophotovoltaic devices will be operated at high intensities and as a result, free carrier concentrations will be quite high. It is not reasonable to ignore free carrier effects in these devices, particularly if the devices depend upon reflection of long wavelength radiation from the back surface and multiple transits of the base region by long wavelength radiation (light trapping effects).

2.1.5 Illumination Spectra

A number of specific illumination spectra are of interest in thermophotovoltaic devices, perhaps the most common of these is that of blackbody radiation. A model was developed for blackbody radiation at arbitrary temperatures and intensities. In addition, for purposes of possible use of these cells in optically stacked configurations a routine was written for the use of filtered illumination, whereby the blackbody radiation or any other illumination source, could be passed through another photovoltaic cell (such as gallium arsenide or silicon) before reaching the germanium cell.

2.1.6 Position Dependent Lifetimes

In general, the minority carrier lifetime will be a function of position as a result of the dependence of lifetime on doping density, and, in the case of ion implanted cells, its dependence on residual damage in implanted regions. The code was suitably modified to allow for doping dependence and damage dependence of minority carrier lifetime.

2.2 Comments on the Germanium Implementation of SCAP1D

This program was run on a CDC 6600 computer. It contains some site specific coding and therefore will probably not run on other machines or at other sites without some modification of the Fortran code.

The input uses a default procedure whereby all parameters have a specified default value. The user simply modifies those values which do not agree with the case which he wishes to study. Since the input program is relatively short, this program can quite easily be run over phone lines from a remote site. The output is easily retrievable by modem over phone lines, with the exception of the graphical output. Extensive graphing routines are available which allow one to plot most microscopic parameters of interest in cell, as a function of operating conditions and position. The plotting routines are site specific and are not accessible remotely. The plotting program can be submitted remotely, but a hard copy would need to be mailed to the user.

2.2.1 Typical Input and Output

In Table 2.1 we show a typical input deck for a thermophotovoltaic cell operating from a 1500 °K blackbody. In Table 2.2 we show an example of the output resulting from this input deck, the output includes open circuit voltage, short circuit current, fill factor, collection efficiency, cell operating efficiency as well as current-voltage characteristics. Had it been specified, we could also have computed the spectral response or the dark current-voltage operating characteristics for this same device. In figures 1-13 we show examples of the graphical output. These examples have been selected from two different runs in order to illustrate the wide variety of plots which are available. These plots are particularly useful in analyzing limitations of the cell and are helpful in suggesting design procedures for minimizing these limitations.

Figure 2.1 is a plot of the current density as a function of voltage for the device described in Tables 2.1 and 2.2. This device was illuminated with a 1500 °K blackbody spectrum, with an incident power of 28.7 watts cm^{-2}. It has an open circuit voltage of .35 volts and a short circuit current of 4.51 amp cm^{-2}. The conversion efficiency is 4.06% while the fill factor is .74 and the collection efficiency is .73%.

In Figure 2.2, the solid line represents the generation rate in hole-electron pairs $cm^{-3}s^{-1}$ as a function of position in the device. The dashed line illustrates the integrated generation, starting at the surface.

Figure 2.3 is a plot of the recombination rate and the integrated recombination as a function of position for the device of Figures 2.1 and 2.2 operating at short circuit conditions. The solid line is the total recombination rate while the dashed line, immediately adjacent to the solid line, is the recombination rate due to HRS recombination. The difference between the two curves is a measure of the Auger recombination. The large dashed line is the integral of the recombination normalized to the total recombination. This plot shows only the first .23 μm of a cell.

Figure 2.4 shows the mobility for electrons (dashed line) and holes (solid line) in the vicinity of the emitter. The mobility is a function of doping and, as a consequence, is significantly reduced in the emitter. The device illustrated in Figure 2.4 and the following figures, is a different device from that shown in Figures 2.1 through 2.3.

Figure 2.5 shows the doping density as a function of position in the vicinity of the emitter. This device has an n-type emitter and a p type base. The sign change is not apparent because of the use of a logarithmic scale.

Figure 2.6 shows the carrier concentration for holes (solid line) and electrons (dashed line).

Figure 2.7 is a plot of the excess carriers as a function of position. In this case the device has been forward biased to 0.1 volts and we have illustrated the excess carrier concentration in the vicinity of the junction. There are very large changes in the carrier concentration at the edges of the space charged region due to the forward bias. Again, the dashed lines indicate electrons while the solid lines indicate holes.

In Figure 2.8, a band diagram for the device, again operating at 0.1 volt forward bias, is shown. This plot shows the conduction band edge, the valance band edge, the center of the gap, and the quasi-fermi level for electrons and holes, all as a function of position.

Figure 2.9. This figure shows the potential as a function of position in the emitter region of the device. The solid line is the potential at a bias of 0.1 volts while the dashed line is the potential distribution under equilibrium conditions.

Table 2.1
Sample Program Input

```
 1  TITLE BLACKBODY RUN FOR DEVICE 9001 TEMP=1500
 2  $
 3  GRID DEPTH=280. MAXN=250 AUTO SOLAR=TRUE
 4  $
 5  RECOM AUGER=TRUE TAUN=.5E-6 ZKN=1.0E15
    +     OHMIC=BACK TAUF=.5E-6 ZKP-1.0E15
    +     SF=0.0 X=.23 FF=0
 6  RECOM X=.345 FF=0 TAUN=13.E=6 TAUF=13.E-6
 7  RECOM X=280. TAUN=1.E-3 TAUP=1.E-3 FF=0
 8  $
 9  OUTPUT EQTBL DEBUG=5 RUN=9007
10  $
11  PROFIL DBULK=-2.29E17 TYPE-GAUSSIAN XJF=.280 XJB=.26
    +     XGF1=.075 XPF1-.03 GPF1=2.74E20
    +     XGF2=.280 XPF2=.08 GPF2=2.86E20
    +     XGB1=.26 XPB1=0.0 GPB1=-3.E20
12  $
13  MATL  TYPE=GE BGN=MAHAN
14  $
15  BIAS VSTART=0.0 VSTOP=.4 VINC=.04
16  $
17  SOLN ITMAX=50 DELMAX=1.E-6 QITMAX=200
18  $
19  SPEC GEFC=TRUE REACK=0.63 TYPE-BBODY TEMP=1500. PWRINC=28.7
20  $
21  ANAL TYPE=SOLAR TEMP=22. AREA=.25
22  $
23  END SLOT=1300 W=SAFE
```

RUN NUMBER 9007 DATE - 10/14/84 TIME - 14.23.46 PROGRAM SCAF1D: VERSION JLG-1

COMMENT: BALCKBCDY RUN FOR DEVICE 9001 TEMP=1500

DOPING PROFIL: GAUSSIAN

DOPING DENSITY (ND-NA) PER CM3 = 1.029E+20 AT X= 0 MICRONS; -3.002E+2(AT X= 280.00 MICRONS

JUNCTION DEPTH= .28 MICRONS BULK DOPING=-2.290E+17 BULK RESISTIVITY= .031 OHM-CM

LAYER: 1 SHEET RESISTANCE = 12.142
LAYER: 2 SHEET RESISTANCE = 1.054

TEMPERATURE= 22.00 C DEVICE LENGTH= 280.00 MICRONS NUMBER OF MESH FOINTS= 250

OPTICAL GENERATION RATE: BBODY SOLAR CONCENTRATION= 1.00 TIMES SHADOW= 0

INCIDENT POWER= 28.70000 WATTS/CM2 GENERATED CARRIERS/INCIDENT PHOTONS= .23285

BACK CONTACT OHMIC, SF= 0 CM/SEC

MINORITY CARRIER LIFETIMES: TAUP= 1.000E-03 SEC TAUN= 1.000E-03 SEC
 CHECK INPUT DECK FOR POSITION DEPENDENCE

SHR TRAP LEVEL: (ET-EV)= .3300 EV

NORMALIZATION FACTORS: VNOR= 2.54333E-02 XNOR= 1.13789E-04
 CARNOR= 1.73688E+13 GRNOR= 1.34143E+21
 TIMENOR= 1.29480E-08 CURNOR= 2.44545E-02

SOLAR CELL PARAMETERS: JSC= 4.50676E+00 VCC= .34978 VMF= .28103
 EFFICIENCY= .0406 FILL FACTOR= .7396 COLLECTION EFFICIENCY= .7322
 RS= 0 CELL AREA= 2.5000E-01 CM2 VBI= .7595

VOLTAGE	TERMINAL VOLTAGE	CURRENT DENSITY (AMPS/CM2)	CURRENT (AMPS)
0	0	4.50676E+00	1.12669E+00
.04000	.04000	4.50656E+00	1.12664E+00
.08000	.08000	4.50619E+00	1.12655E+00
.12000	.12000	4.50523E+00	1.12631E+00
.16000	.16000	4.50194E+00	1.12549E+00
.20000	.20000	4.48862E+00	1.12215E+00
.24000	.24000	4.42996E+00	1.10749E+00
.28000	.28000	4.16264E+00	1.04066E+00
.32000	.32000	2.95944E+00	7.39860E-01
.34000	.34000	1.30573E+00	3.26432E-01
.36000	.36000	-1.84821E+00	-4.62051E-01
.34978	.34978	1.40425E-05	3.51063E-06
.28103	.28103	4.14900E+00	1.03725E+00

Table 2.2

Sample Program Output

Figure 2.10 is a plot of the difference between the potential distribution under 0.1 volt forward bias and the equilibrium value. This plot is useful to show where the voltage is developed within the photovoltaic cell. In this case, it is almost entirely in the vicinity of the space charge region.

Figure 2.11 is a plot of the charge density as a function of position. Again, the solid line shows the charge density under an operating condition of 0.1 volts while the dashed line is the equilibrium charge distribution.

Figure 2.12 shows the electric field in the vicinity of the emitter and space charged region for equilibrium and at a condition of 0.1 volts forward bias.

Figure 2.13 illustrates the hole (solid line) and electron current densities (dash line) as a function of position.

2.3 Use of the Code

In Chapter 5 we will discuss the use of the germanium version of SCAP1D to fit the experimental data obtained from cells which were fabricated under this study. We find that by suitably accounting for surface recombination and implant damage, the computed and experimental values are in excellent agreement. This leads one to develop a relatively high degree of confidence in the results of the computer code. In Chapter 6 we use the parameters developed in Chapter 5 to examine the effects of various potential improvements in device fabrication upon the performance of a TPV cell. The code is first used to optimize the design of the TPV cell and then is used to predict the performance of this optimized cell under various assumptions about operating conditions.

2.4 References

1. G. D. Mahan, Phys. Rev. B, vol. 5, p. 594, 1972.

2. H. P. D. Lanyon and Richard A. Tuft, "Band gap Narrowing in Moderately to Heavily Doped Silicon," *IEEE Trans. on Electron Devices* 26(7), pp. 1014-1018 (1979).

3. P. T. Landsberg, A. Neugroschel, F. A. Liudholm, and C. T. Sah, "A Simple Model for Band-Gap Shrinkage in Silicon," 17th IEEE Photovoltaic Specialists Conference, Kissimmee, FL, May 1-4, 1984, pp. 415-420.
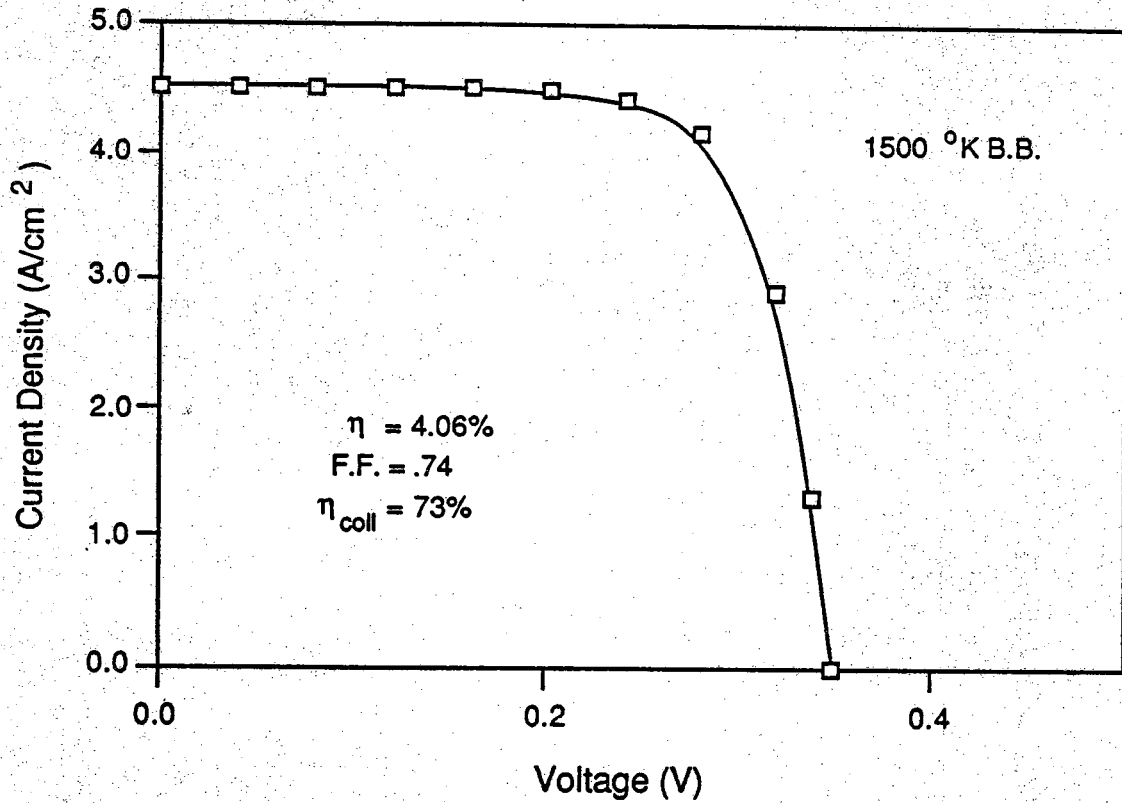
Figure 2.1.   Current density as a function of voltage for an ion implanted germanium thermophotovoltaic cell operating under 28.7 watts cm^{-2} illumination from a 1500 ° K blackbody source.

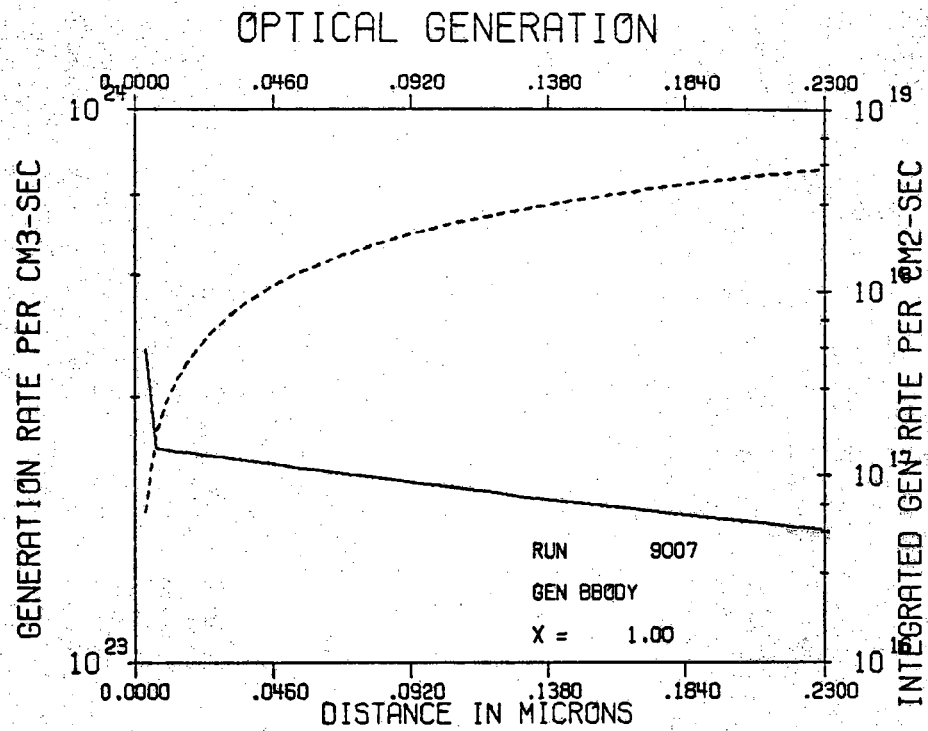Figure 2.2.   Optical generation rate and integrated optical generation rate as a function of position for the germanium thermophotovoltaic cell of Figure 2.1.
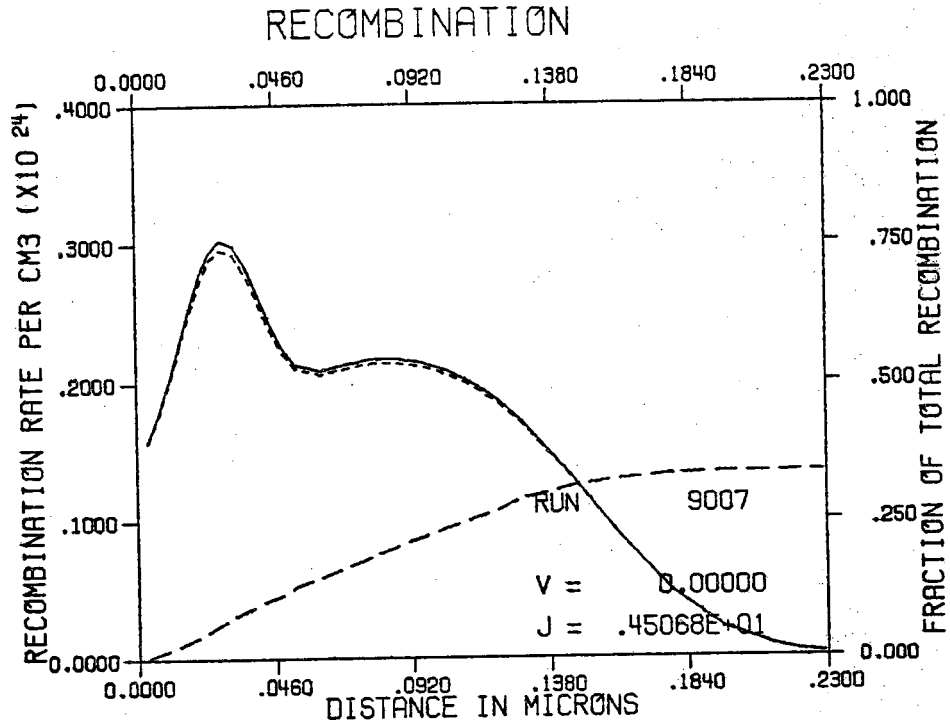
RECOMBINATION

Figure 2.3.   Recombination rate and integrated recombination rate in the vicinity of the emitter for the cell of Figure 2.1 and 2.2.
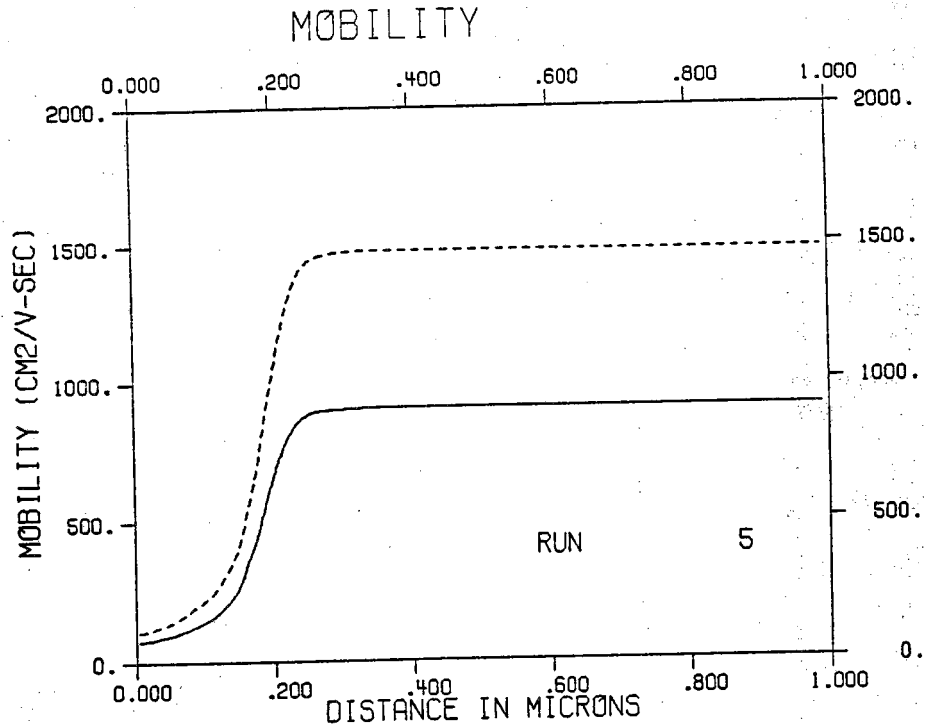
MOBILITY

Figure 2.4.   Mobility as a function of position for holes and electrons.

DOPING (ND-NA)
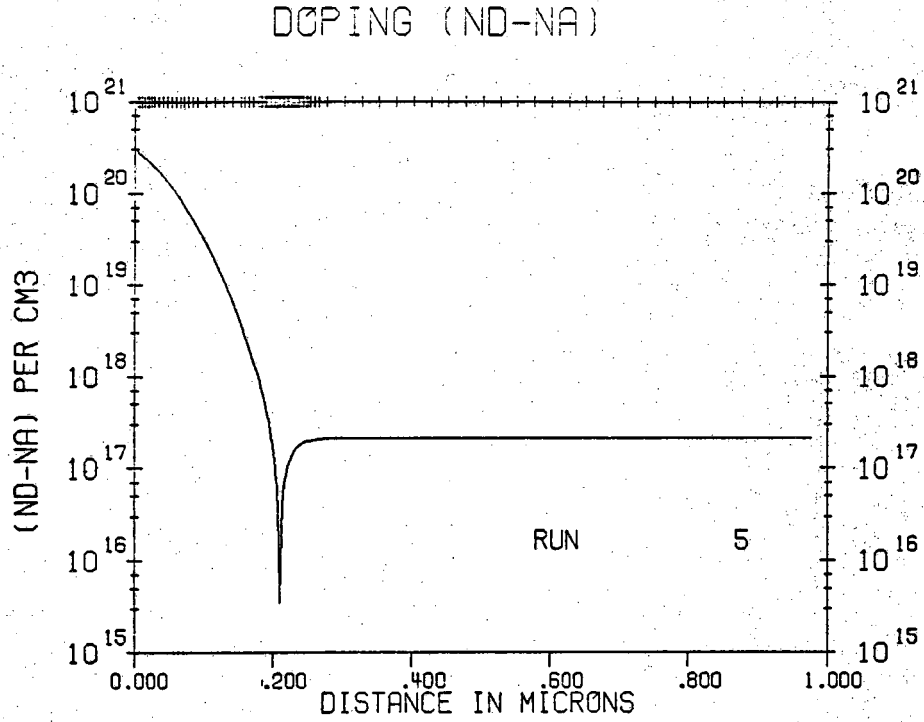
Figure 2.5.   Doping as a function of position. The tick marks at the top of the figure indicate the placement of nodes for the numerical analysis.
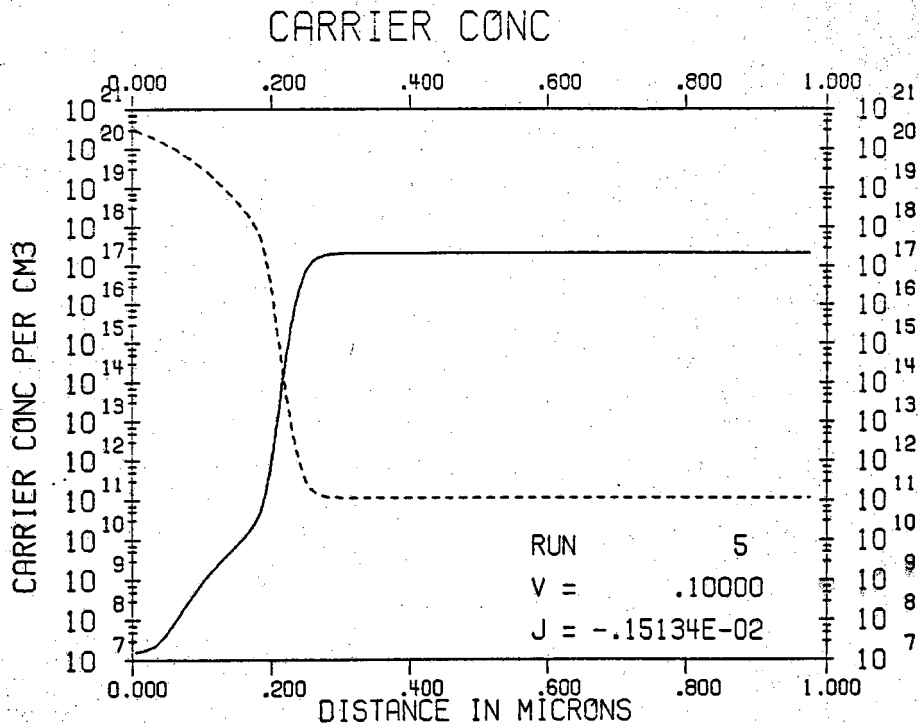
CARRIER CONC

Figure 2.6.   Carrier concentration as a function of position.
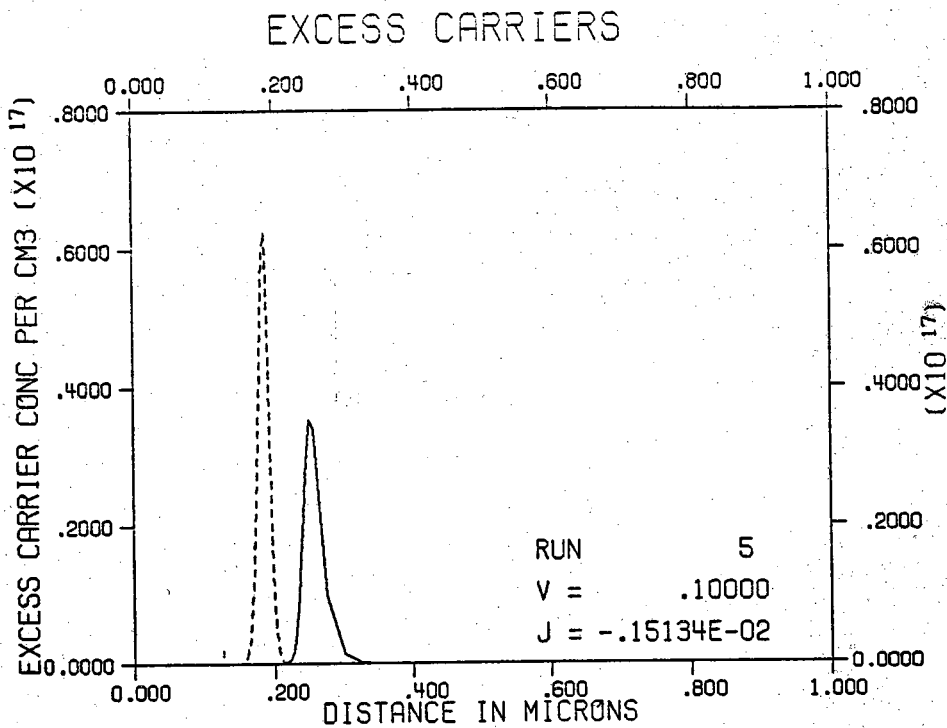
EXCESS CARRIERS

Figure 2.7.   Excess carrier concentration as a function of position.
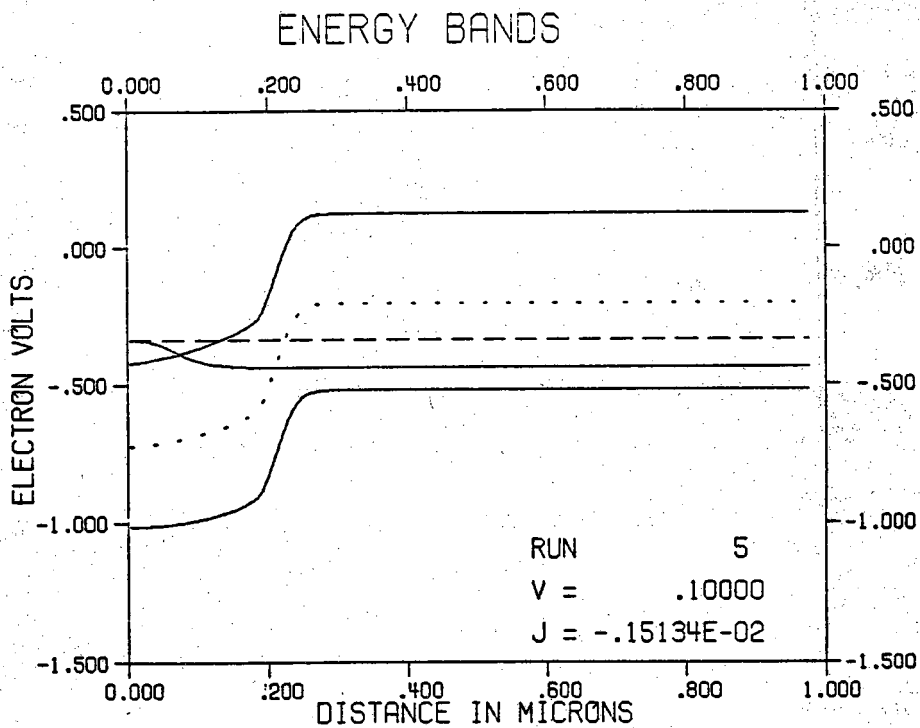
ENERGY BANDS

Figure 2.8.   Energy band diagram and the location of quasi-fermi levels as a function of position.
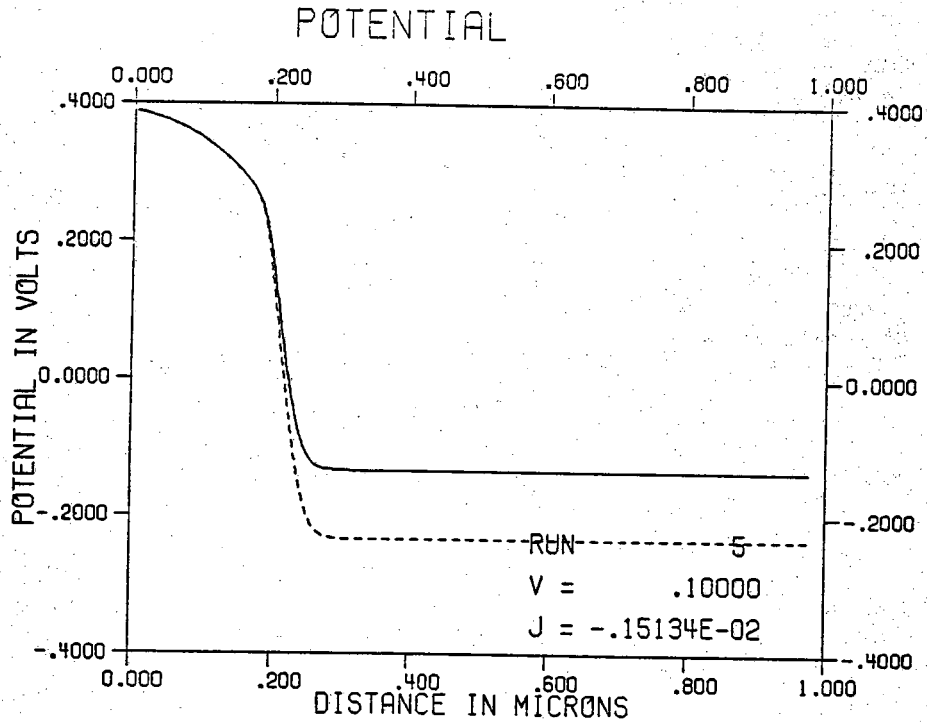
POTENTIAL

Figure 2.9.   Potential and equilibrium potential as a function of position.

V – V(EQ)
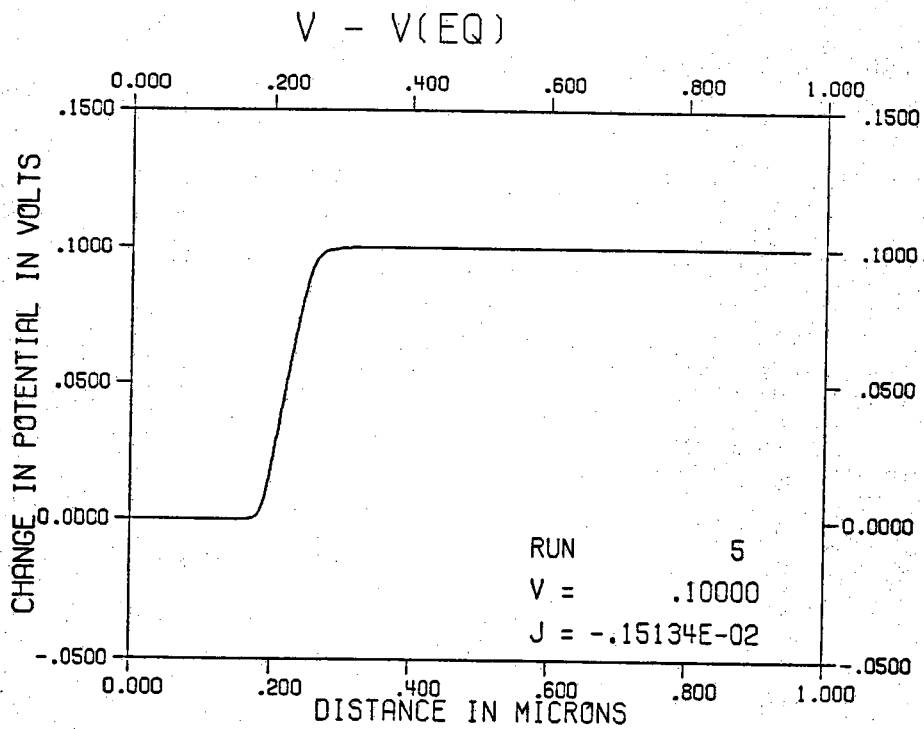
Figure 2.10.   Change in potential as a function of position.
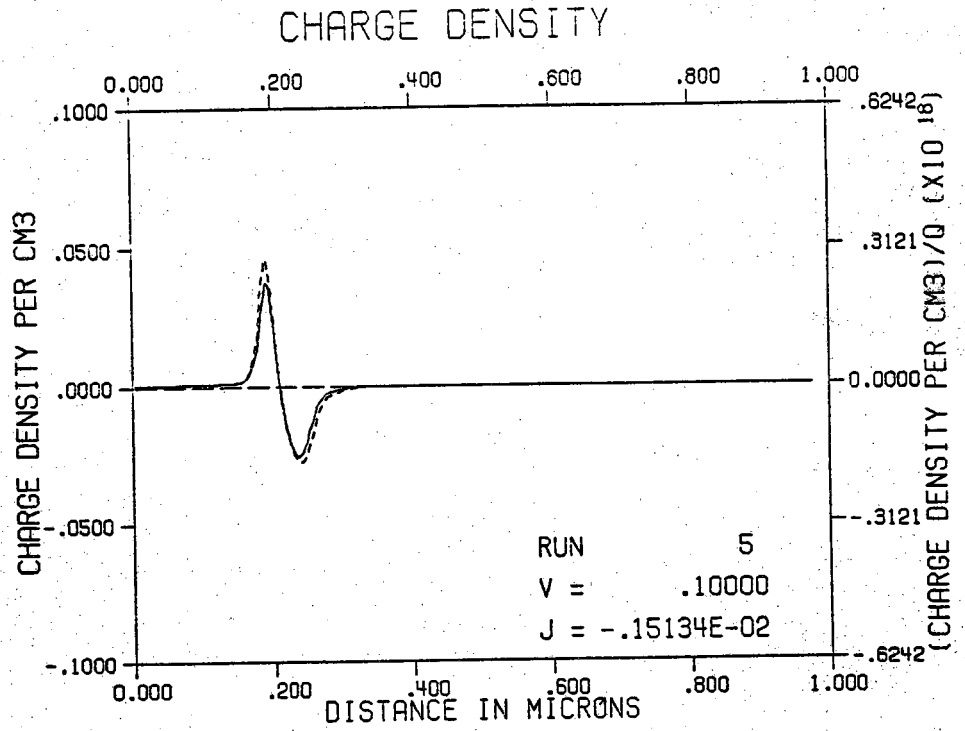
CHARGE DENSITY

Figure 2.11.   Charge density as a function of position.
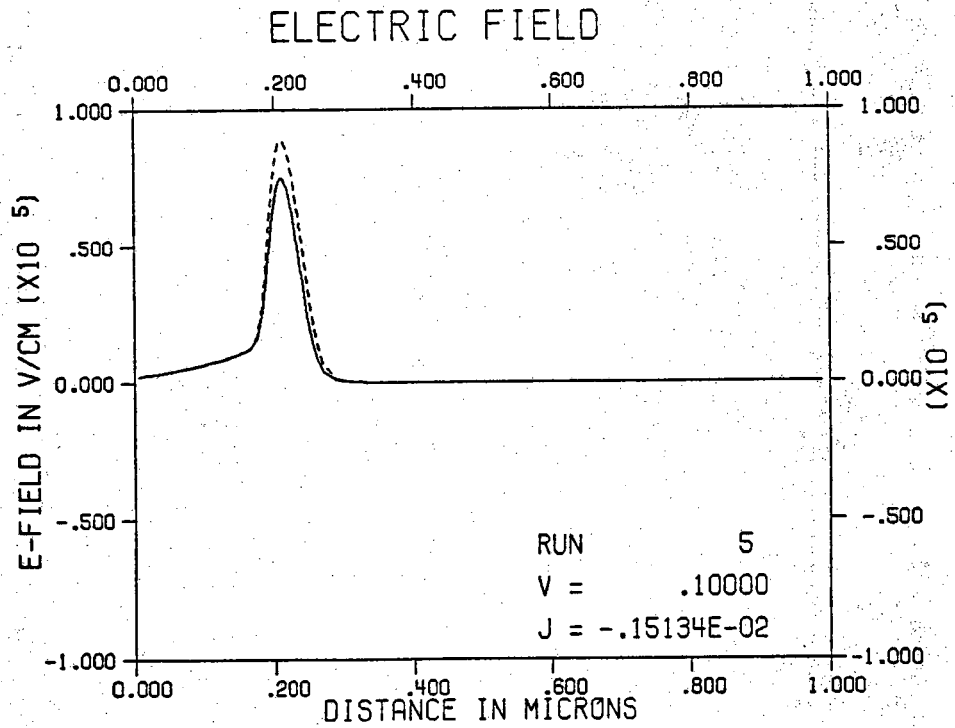
ELECTRIC FIELD

Figure 2.12.   Electric field as a function of position.
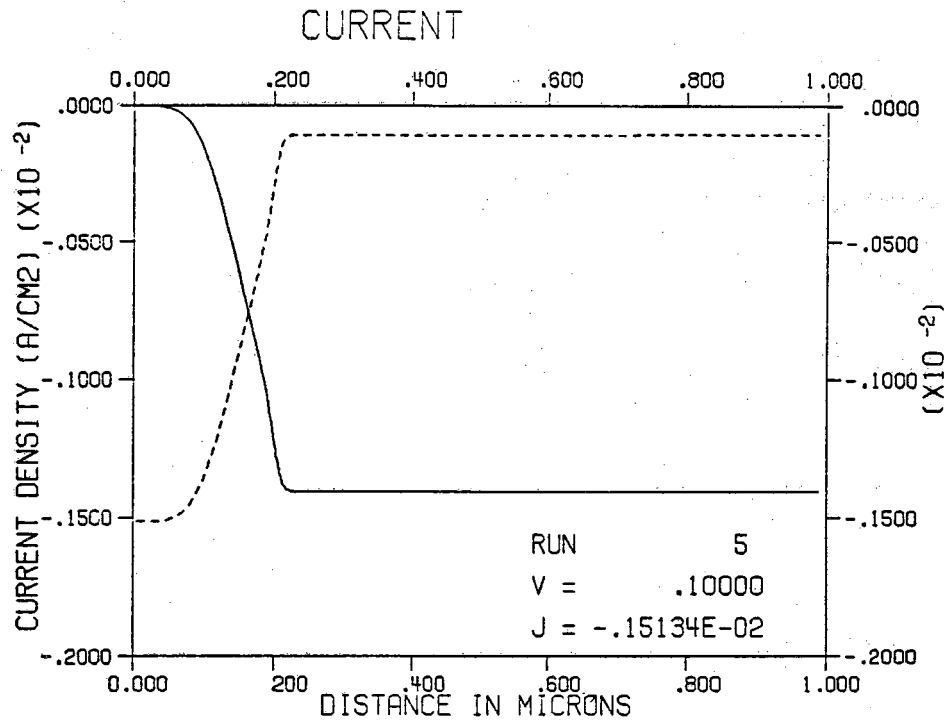
CURRENT

Figure 2.13.   Current density for holes and electrons as a function of position.

CHAPTER 3

FABRICATION OF GERMANIUM TPV PHOTODIODES

In this chapter, procedures for the fabrication of Ge photodiodes are discussed. The fabrication processes are adaptations of existing Si planar monolithic techniques.

3.1 Wafers

The Ge wafers were p-type, (111) orientation, 2" diameter, and had resistivities ranging from 0.1 to 40 Ω-cm. The thickness of the wafers was 300 μm. Both sides of the wafers were chemically and mechanically polished.

3.2 Oxide Deposition

Surface passivation is very important for this device. Imperfections and impurities on the Ge surface serve as a source of the generation-recombination centers. The surface recombination velocity, S, is extremely sensitive to surface conditions which are strongly influenced by materials deposited on the surface. For silicon devices, the native SiO_2 film serves as a passivation layer. In addition, this passivation film is also used as an insulating layer, as diffusion and ion-implantation mask, and as a capping layer over doped regions to prevent outdiffusion during thermal annealing cycles. Unfortunately, the oxides of germanium which form at atmospheric pressure are not suitable for these purposes.

GeO_2 has the serious disadvantage of being water soluble. This causes unstabilities in many cleaning and etching steps which are necessary for planar fabrication. This problem also prevents its use as an effective passivation agent because of the presence of moisture in the atmosphere.

Many films, including SiO_2, Si_3N_4, Al_2O_3 and combinations of these materials have been the subject of intensive study. [1] These films were compared with respect to their etch rate, dopant masking capabilities, mechanical stress, and oxygen and water permeability. SiO_2 was proven to have the most favorable properties. SiO_2 is effective not only for masking against ion implantation, but also in reducing the surface state density at the SiO_2–Ge interface.

We have investigated two methods for SiO_2 deposition on Ge: sputter deposition and chemical vapor deposition (CVD).

3.2.1 Sputtered SiO_2

The sputter deposition is undertaken at room temperature using an ion mill technique. This film was found to be uniform over the entire wafer. However, there are several disadvantages which limit its application:

(1) The growth rate of the sputtered film is slow. The typical deposition rate is less than 100 Å min. It takes about 90 minutes to grow a 8000 Å film. This thickness is required to effectively mask the ion implanted impurities.

(2) A complicated mixture of Si, Ge, and O was formed at the SiO_2-Ge interface. This Si-Ge-O mixture is difficult to remove and therefore produces problems in processing.

3.2.2 Chemical Vapor Deposition (CVD)

Many other methods are available for the deposition of SiO_2 films. However, CVD techniques are frequently used in semiconductor processing because of the relative ease of deposition and the high quality of the resulting films.

The deposition of SiO_2 by reacting dichlorosilane with nitrous oxide at 900°C at low pressure is given by

$$SiCl_2H_2 + 2N_2O \rightarrow SiO_2 + 2N_2 + 2HCl$$
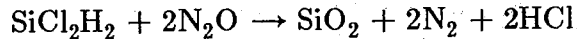
This method gives excellent quality SiO_2 with good uniformity. However, the reaction takes place at 900°C which is too close to the melting point of Ge (950°C).

The decomposition of tetraethoxysilane, $Si(OC_2H_5)_4$, (TEOS), in a low pressure reactor is another common technique for depositing SiO_2 films. The processing takes place at 650 to 750°C with the following reaction

$$Si(OC_2H_5)_4 \rightarrow SiO_2 + byproducts$$
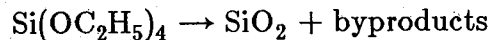
The advantage of TEOS deposition are excellent uniformity, conformal step coverage, and good film quality. The disadvantages are the high-temperature process and liquid source requirements.

In this work, the SiO_2 films were formed by reacting silane and oxygen at a temperature of 400°C. The main advantages of the silane-oxygen reaction are the relatively low deposition temperature, and the fact that the deposition can be carried out at atmospheric pressure. The SiO_2 layer is formed on the surface of a wafer placed on a hot plate heated to 400°C. The chemical reaction is as follows:

$$SiH_4 \text{ (gas)} + 2O_2 \text{ (gas)} \rightarrow SiO_2 \text{ (solid)} + 2H_2O \text{ (gas)}$$
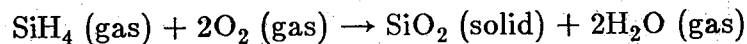
3.3 Ion Implantation Techniques and Annealing

The p^+ channel stop, the high-low junction, and n^+ emitter are formed by ion implantation. The use of implantation techniques has several advantages over diffusion methods. In the ion implantation process, the doping parameters can be precisely controlled by the external systems rather than by the physical properties of the substrate. For example, the beam energy can be used to control the depth of the p-n junctions, and the ion dosage concentration can be used to control the doping profiles.

3.3.1 Impurities

For a high quantum efficiency n^+pp^+ photodiode, a shallow n^+ emitter region is essential. Arsenic ions produce a small projected range, R_p, when implanted into a Ge substrate. Small R_p yields a shallow n^+ junction. Since the diffusivity coefficient of As in Ge is relatively small, the arsenic layer can be annealed at a high temperature with very little change in doping profile.

Phosphorus can be used as a n^+ dopant for a deep junction because of its light atomic weight and deeper projected range. However, increasing the phosphorus dose requires increasingly higher annealing temperatures. Moreover, in heavily phosphorus-doped Ge samples, annealling caused cracking on the surface and, thus, higher leakage current. This cracking was severe enough that phosphorus doping does not appear to be feasible for these devices.

Boron is used as the p^+ dopant for the channel stop on the front surface and the high-low junction on the back of the device. Since the B^+ implantation at room temperature does not produce amorphous layers, high temperature annealing is required. In addition, the channeling effect is more severe for the light B^+ ion. This problem can be alleviated by using the molecular species BF_2. The heavy BF_2 ion creates an amorphous zone on the bombarded areas, and the disassociation of B and F upon the atomic scattering gives a low energy boron dosage and thus shallow junctions.

3.3.2 Ion Implant Annealing

The ion implantation process produces considerable lattice damage. This damage results in a degradation of mobility and minority carrier lifetime. In addition, only part of the implanted ions reside in substitutional sites, where they are electrically active. Practical thermal anneal cycles can only partially remove the lattice damage. Therefore, the minority carrier lifetime in the implanted region is much shorter than that in the base region.

In the fabrication of the germanium diode, the post-implantation anneal is essential to bring the impurities to the proper lattice sites. The conventional approach is to anneal the implanted samples in the high temperature furnace. This high annealing temperature and relatively long annealing time slightly changes the profiles of the implanted impurities. Flash anneal, on the other hand, provides a high temperature environment in a very short period of time, sometimes in seconds, with little change in the doping profile.

A study was performed to compare these two techniques. Experiment results showed no difference in the properties of cells fabricated using the two methods.

Figures 3.1 and 3.2 show spreading resistance plots of the implanted As profile for a shallow ($.5\mu$m) and a deep (1.3μm) junction. The shallow profile was used for the active portion of the emitter, while the deep implant was used under the metal contacts to help reduce shorting problems encountered with shallow emitters.
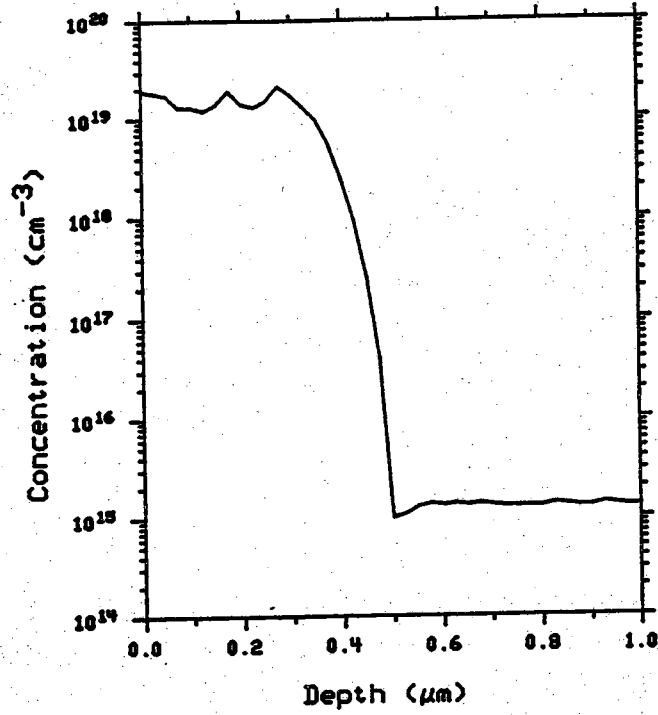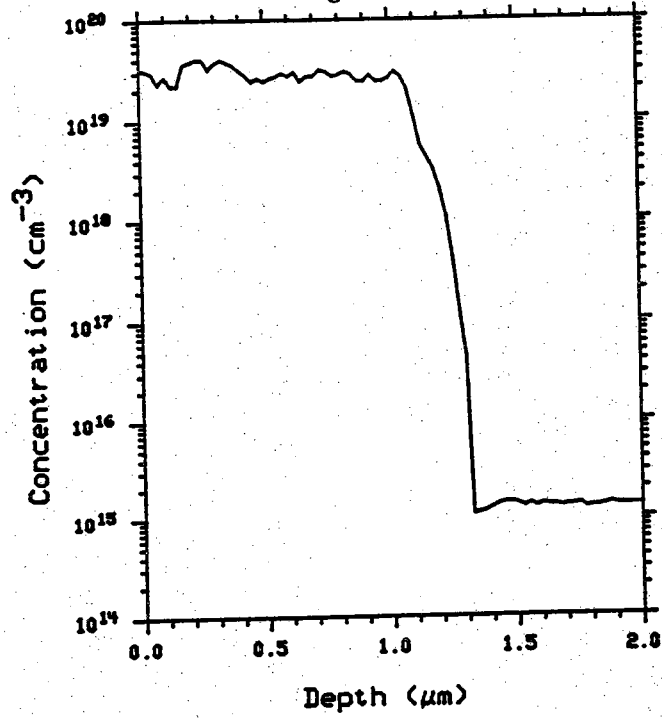
Figure 3.1

Figure 3.2
Deep Implanted As profile

3.4 Metalization

The high intensity operation of TPV cells requires high quality metalization which in turn requires low-resistance interconnections, and low-resistance contacts to n^+ and p^+ semiconductors. In addition, the metal adherence should be high, and electromigration and corrosion should be low.

A three layer Ti/Pd/Ag metal was used for the contacts. The Ti (500Å) makes a low resistance ohmic contact to the germanium and the Ag (1000-3000Å) provides electrical conductivity. The Pd (500Å) in the middle prevents an oxidation of the Ti. This is the conventional metal contact system used in high quality silicon solar cells.

This system was observed to provide good low resistive contact to the Ge when suitability annealed. Schottky barriers were observed on some occasions if the contacts were not annealed.

An ion beam sputter technique was used for metal deposition. Sputter metalization is a clean process and the thickness of the metal layer can be precisely controlled.

3.4.1 Sputtering System

The sputtering system used in our research was the Commonwealth Scientific Ion Millitron. This ion mill has the capability of sputter coating and etching in the same low pressure chamber. The sputtering rate can be controlled by the ion beam current and the duration of the deposition. A typical metal deposition rate was about 100 Å min.

3.4.2 Procedures

The germanium substrate is cleaned before being placed in the deposition chamber. Any residuals remaining in the contact window areas will degrade the metal adhesion and increase contact resistance. The most common cleaning process involves the use of buffered HF to remove the thin residual oxide, followed by an extensive DI water rinse and N_2 blow dry. The substrates are loaded into the ion mill chamber shortly after the cleaning process.

Prior to the metal deposition, the accelerated Argon gas is directed to the substrate for a short period of time (typically, 30 seconds) to sputter etch the surface. The sputter etch will also remove the residual film from the contact window areas and enhance the integrity of the contact between the metal and germanium.

The metal patterns are defined by a lift-off process. In the lift-off process the inverse pattern is formed by lithography using AZ1350 positive photoresist, followed by a metal deposition. The whole wafer is then immensed into a warm acetone solvent and the undesired metal is lifted off the wafer.

3.5 Cell Design

Figure 3.3 show the cross section of an n^+pp^+ germanium diode. Ion implanted arsenic is used to form the shallow emitter active region. The boron-implanted p^+ channel stop prevents lateral current flow, and the p^+ layer on the back of the device forms a high-low junction. CVD SiO_2 is used for passivation and as an ion implantation mask. A three layer Ti/Pd/Ag metal is deposited as described above. The n^+

regions under the metal contacts are implanted deeply (about 1.5 μm) to prevent metal-substrate shorting.

Figure 3.4 is the top view of the diode and various test cells used in this investigation. The photodiode is 2 × 2 mm. Figure 3.5 shows test devices which were used to measure the contact resistance, the resistivity of implanted regions, MOS capacitors to monitor the quality of SiO_2-Ge interfaces, and field effect transistor effects.

3.6 Summary of the Fabrication Process

The fabrication procedures for a germanium photodiode are summarized as followings:

1. Choose the starting material resistivity.
2. Clean the wafers.
3. Deposit SiO_2 on the front surface.
4. Define the area for p^+ channel stops (mask #1).
5. Implant boron on both sides of the wafer.
6. Define the area for the n-guard ring (mask #2).
7. Implant arsenic.
8. Deposit SiO_2.
9. Define the area for n^+ shallow emitters (mask #3).
10. Implant arsenic.
11. Deposit SiO_2.
12. Anneal samples at 650°C for 20 min in an Argon ambient.
13. Define the area for metal contacts (mask #4).
14. Define metal patterns using a lift-off process (mask #5).

3.7 References

1. T. O. Sedgwick, J. A. Aboaf, S. Krongelb, "Passivating, Masking, Mechanical and Electrical Properties of Dielectric Films for Ge-Planar Devices," IBM Research Report, RC 2573 (#12295), 1969.
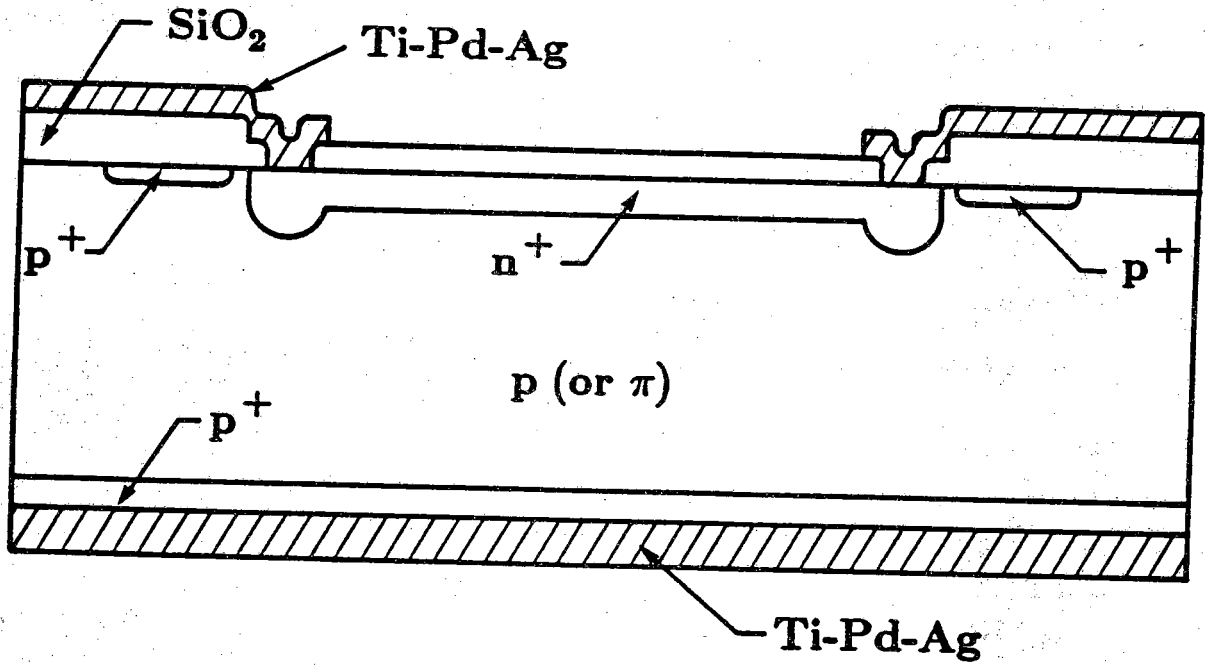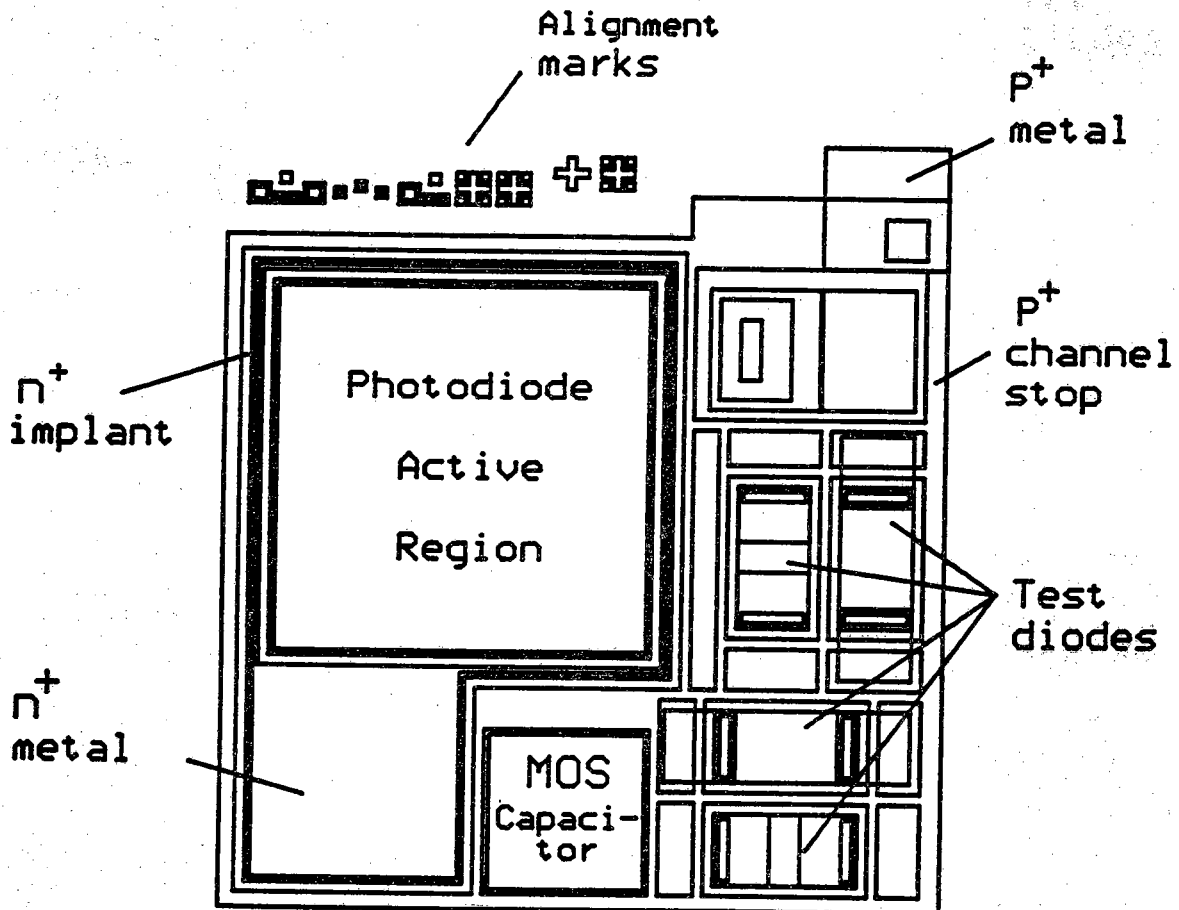
Figure 3.3
n+pp+ TPV Cell

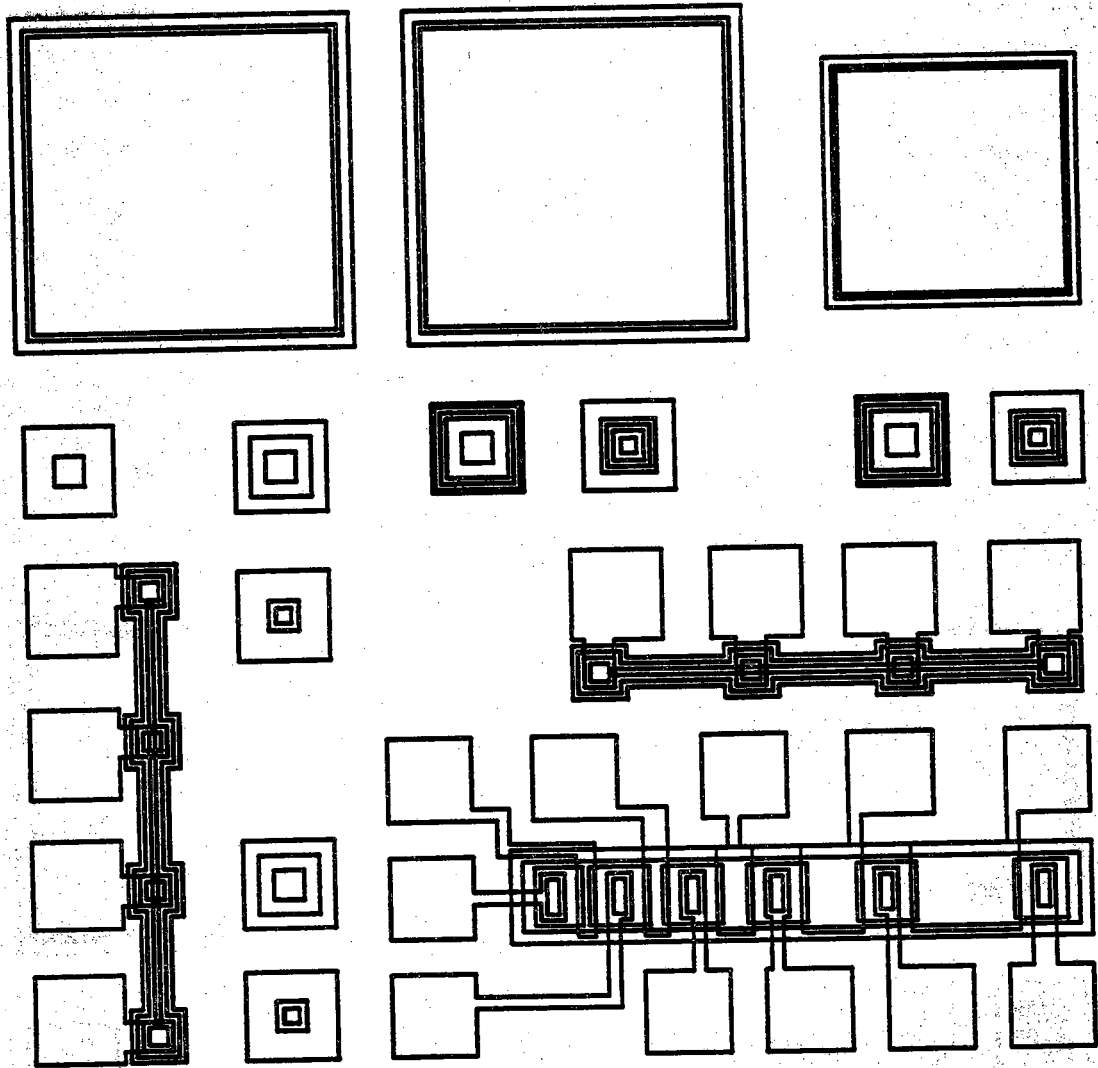Figure 3.4
Top View of Diode and Test Devices

Figure 3.5
Test Devices

CHAPTER 4
EXPERIMENTAL RESULTS

In this chapter, the electrical and optical properties of the n^+pp^+ germanium TPV cell will be studied. The electrical tests were conducted at Purdue University, and the optical tests were conducted at University of Arizona and the National Bureau of Standards.

4.1 Electrical Measurements

The I-V characteristics were taken using a HP4151A Semiconductor Parameter Analyzer, which is a fully automatic instrument designed to measure, analyze, and graphically display the DC parameters and characteristics of diodes.

4.1.1. Dark Current Measurement

The typical dark I-V characteristics are shown in Fig. 4.1a & b. This particular diode was fabricated on a 2 Ω-cm, p-Ge wafer with (111) orientation.

For a diode, with step junction, the dark current can be written as

$$I = I_o \left[\exp[\frac{q}{nkT}(V - IR_s) - 1] \right] \tag{4.1}$$

where n is the ideality factor and R_s is the series resistance. I_o, in the simplest case of no heavy doping effects, is given by

$$I_o = \left[\frac{qn_{io}^2 D_p}{N_D L_p} + \frac{qn_{io}^2 D_n}{N_A L_n} \right] \times (\text{area}) \tag{4.2}$$

where n_{io}, D_p, D_n, L_p, L_n, N_D, and N_A are the intrinsic carrier concentration, the diffusion coefficient, the diffusion length and the doping, respectively.

The saturation current I_o is a function of doping concentration N_A and N_D, and the minority carrier lifetime, which itself is a function of the doping concentration. Figure 4.2 shows the measured saturation current distribution versus the substrate resistivity, which is inversely proportional to the background concentration. As expected the low substrate resistivity cells have low saturation current.

4.1.2. I_{sc}-V_{oc} Measurements

The I-V characteristics for the illuminated diodes can be written as

$$I = I_L - I_o \left[\exp[\frac{q}{nkT}(V - IR_s)] - 1 \right] \tag{4.3}$$

where I_L is the light generated current. To eliminate series resistance effects, the open circuit voltage, V_{oc}, and short circuit current, I_{sc}, were measured by varying the illumination intensities. At the open circuit voltage, where the total current is zero, Eq. (4.3) can be written as

$$I_L \simeq I_{sc} = I_o \left[\exp(\frac{qV_{oc}}{nkT}) - 1 \right] \tag{4.4}$$

In a $\log(I_{sc})$-V_{oc} plot, the intercept with the current axis gives the value of I_o, and the slope of the curve gives the ideality factor n. An ideality factor n of 1.05 is obtained

I (uA)

MARKER(5. 0000V   -15. 42uA   )

80. 00

10. 00
/div

0

-20. 00

7. 000   VF   0   -3. 000
                      1. 000/div   (V)

I (uA)

MARKER(10. 000V , -19. 36uA ,   )

500. 0

100. 0
/div

0

-500. 0

45. 00   VF   0 -5. 000
                      5. 000/div   (V)
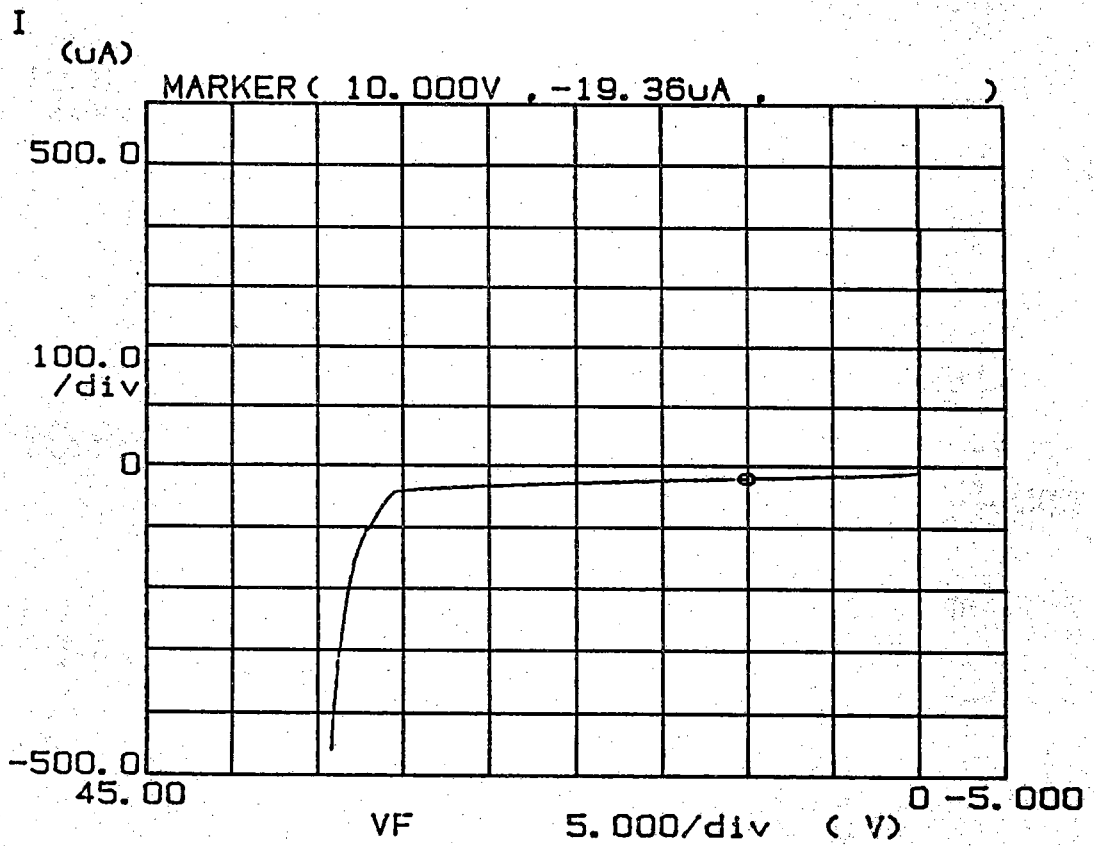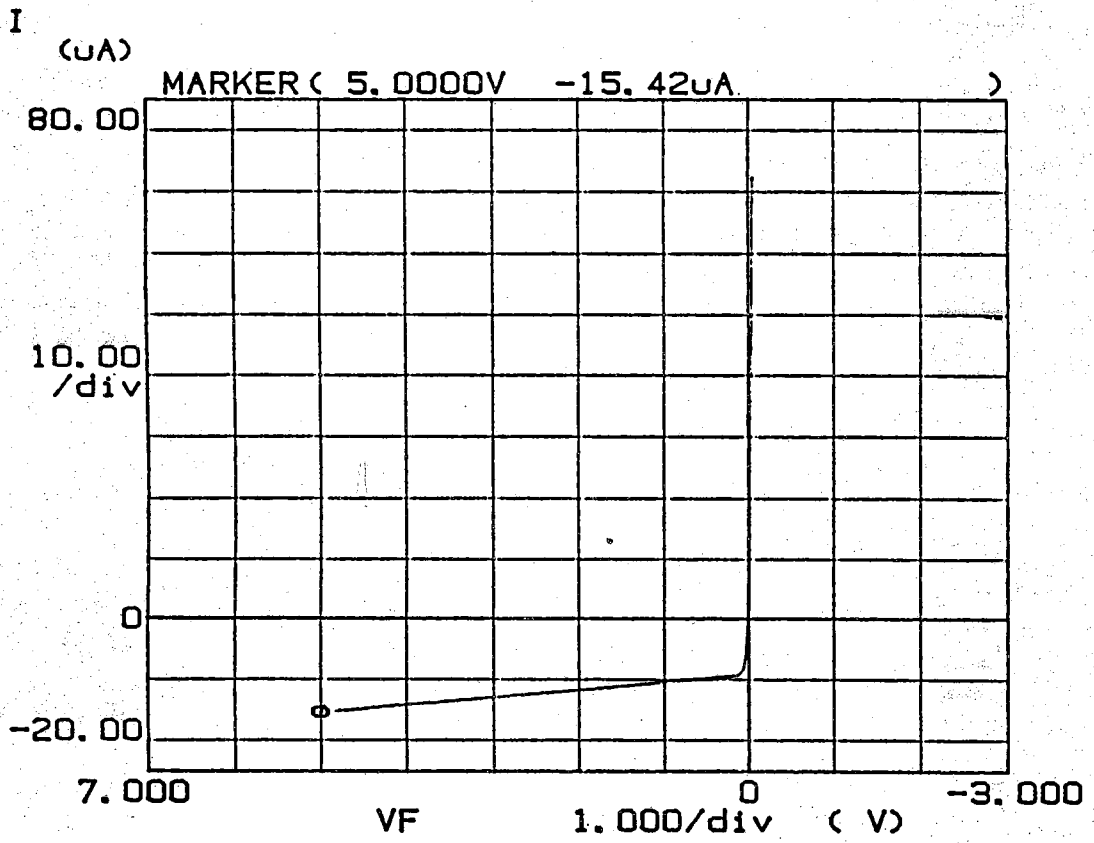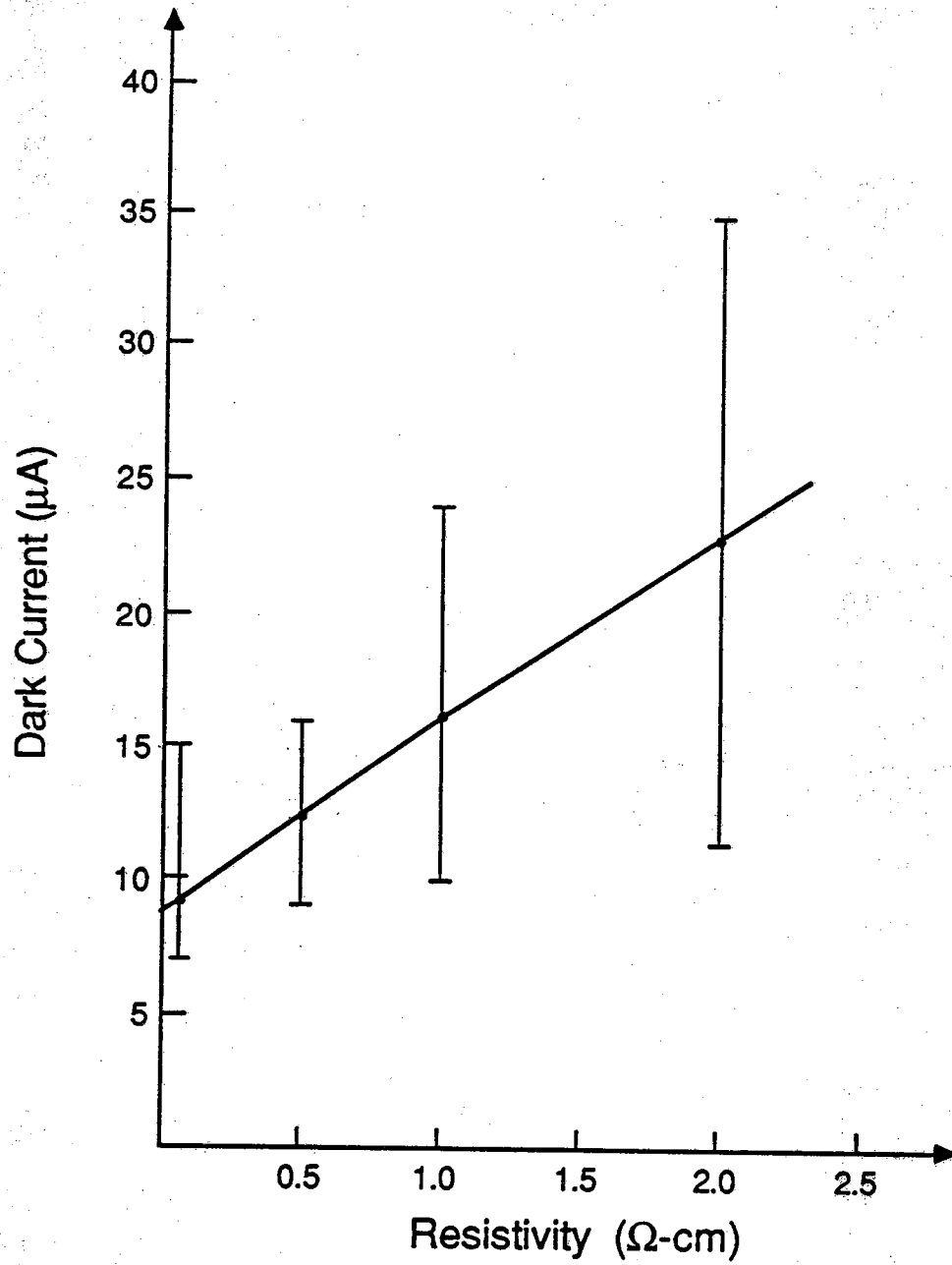
Fig. 4.1   Dark I-V

Fig. 4.2   Saturation current vs substrate resistivity

from the data shown in Fig. 4.3.

4.1.3. Series Resistance R_s

As shown in Fig. 4.3, the deviation of the forward I-V characteristics curve from the I_{sc}—V_{oc} curve indicates the presence of a high series resistance in the cell. The high R_s comes from the shallow n^+ emitter.

4.1.4. CV Measurement

The capacitance-voltage (C-V) measurements were made on the MOS capacitors fabricated along with the cells. The measurement result is shown in Fig. 4.4.

4.2. Optical Measurements

The primary objective of this work is to design and fabricate a high efficiency cell. Therefore, the quantum efficiency is an important characteristic in the cell. Ideally it should approach 100%.

All optical measurements were conducted at the University of Arizona. The measurements include the power of the incident light source, P_{opt}, with frequency, ν, the reflectance, $r(\lambda)$, and the light generated current, I_L. The internal quantum efficiency $\eta(\lambda)$ can be calculated by the following expression,

$$\eta(\lambda) = \frac{I_L/q}{[P_{opt}/h\nu]\,[1 - r(\lambda)]} \tag{4.4}$$

The measured internal quantum efficiency is shown in Fig. 4.5.

The rapid fall of $\eta(\lambda)$ at short wavelengths is due to the carrier losses at the front surface and in the emitter region. The presence of high concentrations of both substitutional and interstitial donors in the emitter region increase the probability of the electron-hole recombination and, therefore, reduces the minority carrier lifetime, τ_p. In addition, the surface states at the SiO_2 — Ge interface create recombination centers. The surface recombination mechanism can be characterized by the surface recombination velocity, S_p. A relatively large S_p and short carrier lifetime have been found in the Ge photodiodes. The typical values for τ_p in the emitter and S_p at the surface are 10^{-8} sec and 10^5 cm/sec respectively. We will discuss this in detail later. For purposes of comparison, the measured quantum efficiency of a diode with an induced junction is also shown in Fig. 4.5. As expected this diode does not exhibit the emitter recombination problems of the implanted diode.

The quantum efficiency is a function of the substrate resistivity as well. Generally speaking, the higher the substrate resistivity, the higher the quantum efficiency will be. However, as we have shown in Fig. 4.2, the saturation current increases as the base resistivity increases. This results in a reduction in the V_{oc}.

Fig. 4.6 shows the measured quantum efficiency for photodiodes with two different base resistivities. DA8-1-1 is a cell with substrate resistivity of 0.1Ω-cm. Its emitter was As doped with a density of $10^{14}/cm^2$ and an energy of 45 Kev. For device DA10-4A-31, the emitter was implanted using the same density but an energy of 30 Kev on a 2 Ω-cm substrate. Higher quantum efficiency in DA10-4A-31 is found at short wavelengths due to the shallow emitter junction depth, and at long wavelengths due to the longer minority carrier lifetime in the base.
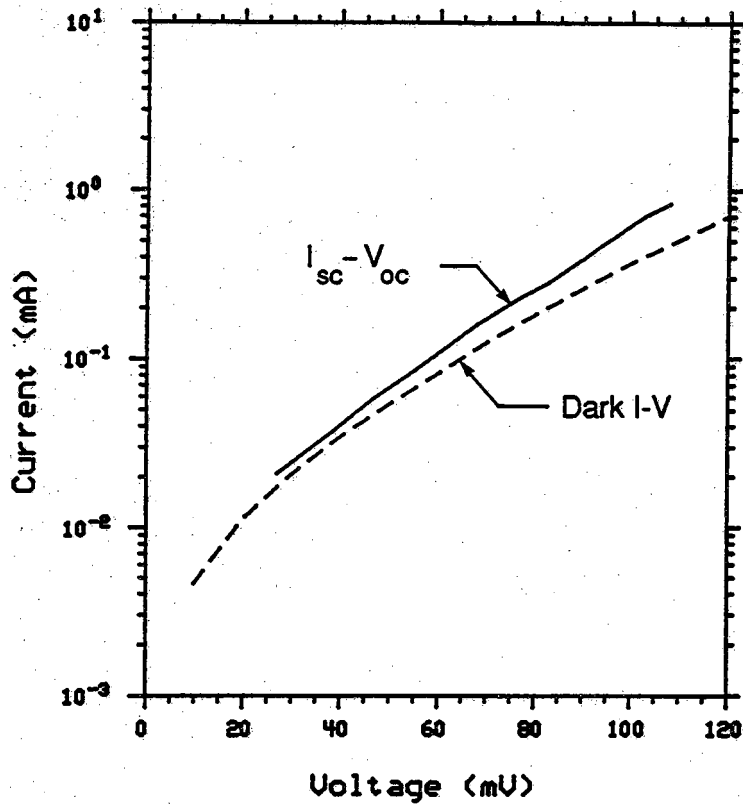
Fig. 4.3   Isc-Voc and dark forward current.
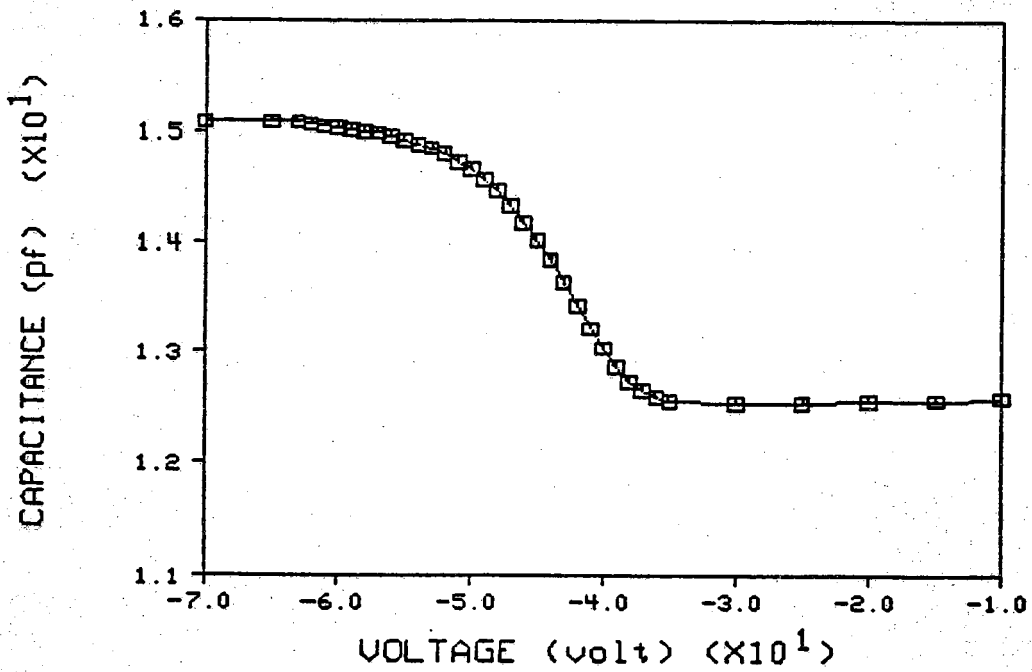
Fig. 4.4   C-V measurement
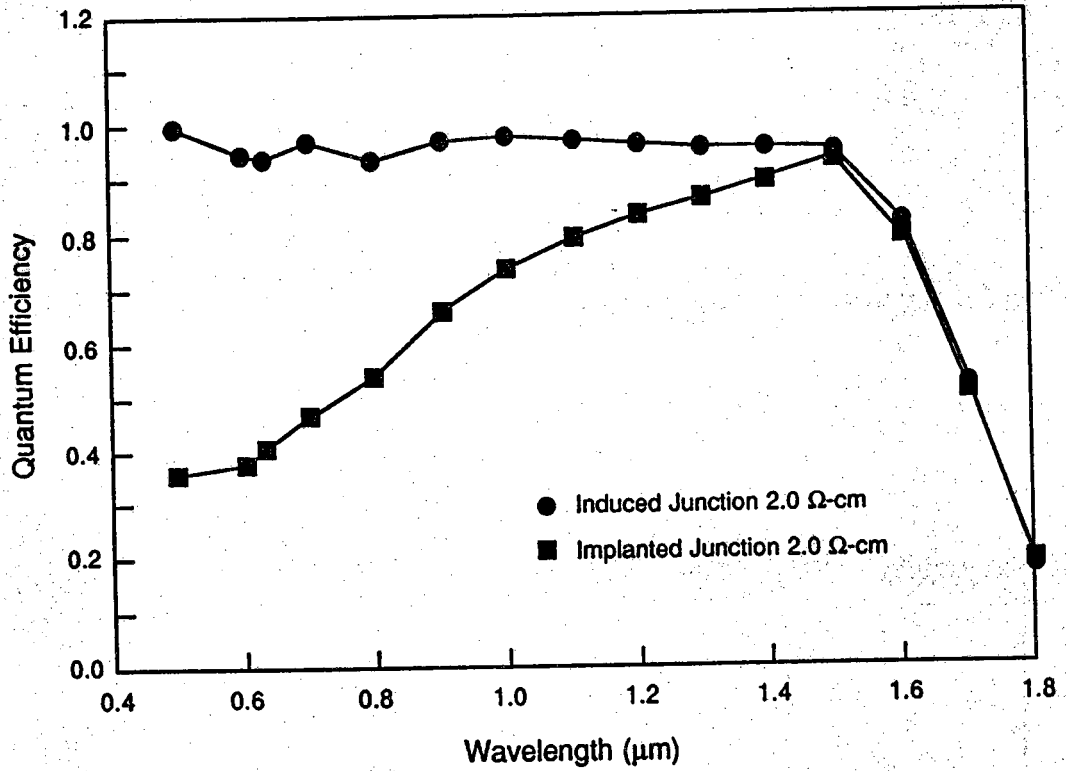
Fig. 4.5   QE vs wavelength
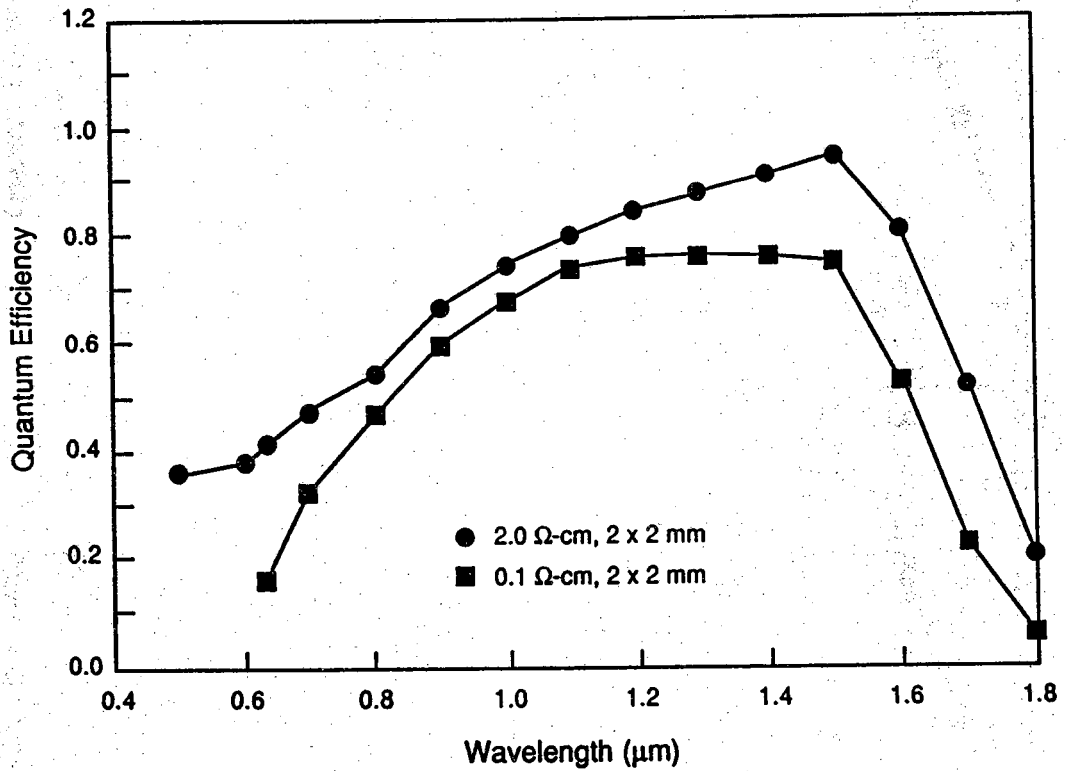
Fig. 4.6   QE vs wavelength for 2.0 ohm cm and 0.1 ohm-cm bases.

Emitter junction depth, x_j, also plays an important role in the quantum efficiency. Fig. 4.7 shows the quantum efficiency of two diodes with the same substrate doping, but different x_j. The shallower emitter results in a higher quantum efficiency.
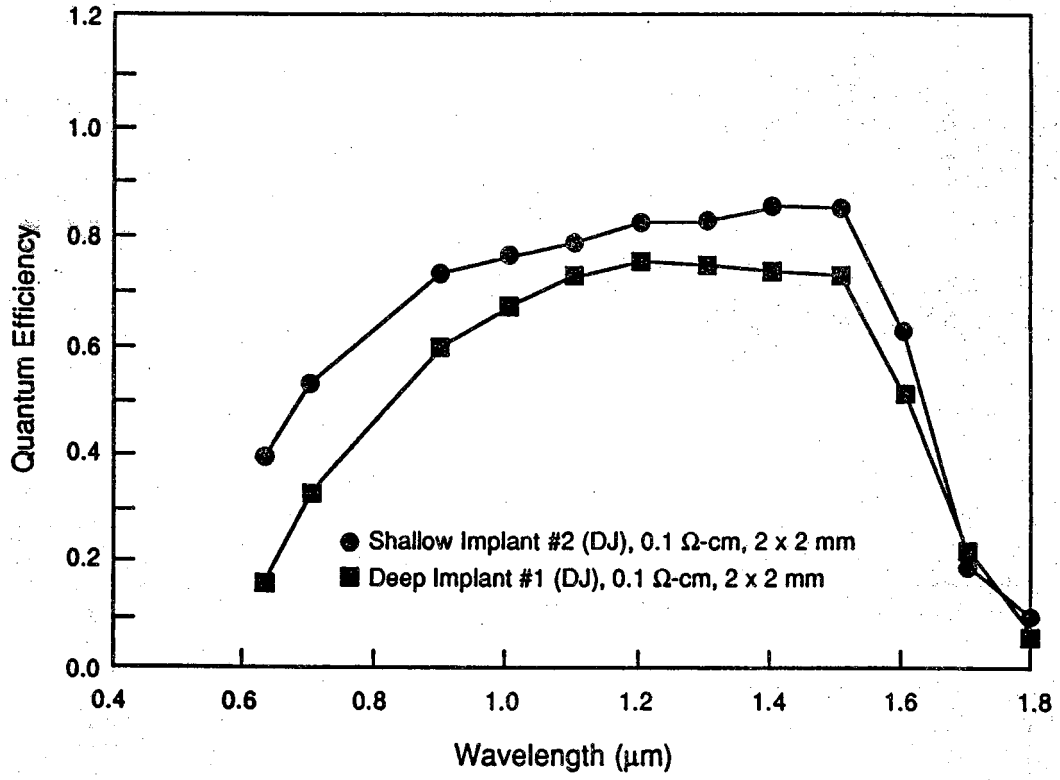
Fig. 4.7   QE vs wavelength for two different junction depth.

CHAPTER 5

COMPUTER SIMULATION OF MEASURED DATA

5.1 Introduction

Using the data obtained from the measurements described in the previous chapter, the computer simulation program SCAP1D was used to model device operation. This chapter describes the methods used to obtain a device model adequate for use as a tool for making projections of the germanium cell operation under various illumination conditions. These projections are given in Chapter 6.

5.2 Measurements Modeled

The computer program SCAP1D used to simulate the fabricated devices is described in Chapter 2. Simulations of various experiments were made in order to construct a reliable model for the germanium cells. These experiments included the internal quantum efficiency of the cell as a function of wavelength, and measurements of forward and reverse current-voltage characteristics in the dark and under illuminated conditions. The model obtained from these simulations is used to aid in the optimization of the cell design and in the projection of device operation under various operating conditions.

5.3 Simulated Device Description

Some of the parameters used in SCAP1D are given in Table 5.1.

Table 5.1

Parameter	Value	Description
DEPTH	280μm	Device thickness
AUGER	ON	Use Auger recombination model
GEFC	ON	Use free carrier absorption model
BGN	MAHAN	Use Mahan band-gap narrowing model
TEMP	22	Device temperature $^\circ$C

Auger recombination and free carrier absorption were utilized since these processes are inherent to the device operation. The band-gap narrowing model of Mahan [1] was chosen to model the band-gap in the heavily doped implanted regions of the device. The temperature was set to that at which the measurements were made. The implanted contact layers were modeled using a gaussian distribution.

5.4 Internal Quantum Efficiency Simulations

The measured internal quantum efficiency is shown in Figure 5.1. These measurements were performed by M. Nofziger at the University of Arizona. The internal quantum efficiency for this measurement is defined as the ratio of the measured current to the incident photon flux, corrected for the magnitude of the reflected photon flux. This definition assumes that all of the incident photon flux is either reflected from the front surface or is absorbed in the semiconductor. At long wavelengths, where the absorption coefficient is small, this assumption will lead to over estimation of the internal quantum efficiency. At these wavelengths the photon flux is not entirely absorbed before it reaches the back surface of the device. Some of the flux will be transmitted through the back (for back surface reflectances less than one) and the remaining flux will be reflected towards the front surface. Subsequent transmission of the reflected flux through the front surface is accounted for in the definition and measurement since the total reflectance of the device is measured. The photon flux assumed to be available, for absorption in the semiconductor, is too large by the amount transmitted through the back.

With the measured current defined as I_{meas}, the measured internal quantum efficiency is given by

$$\eta_{meas} = \frac{I_{meas}}{qI_o(1 - R_F')} \tag{5.1}$$

where R_F' is the measured total reflectance of the device, and I_o is the total incident photon flux in units of photons/cm^2-sec. The computed internal quantum efficiency is given by

$$\eta_{SCAP1D} = \frac{I_{meas}}{qI_o[(1 - R_F)(1 - e^{-\alpha_T L})(1 + R_B e^{-\alpha_T L})]} \tag{5.2}$$

where R_F and R_B are the front and back surface reflectances, α_T is the total absorption coefficient and L is the device thickness. It is observed that $\eta_{SCAP1D} > \eta_{meas}$ for $R_B < 1$.

Once the basic device model has been set, most of the material parameters for the device have been chosen and can not be used to adjust the simulation results to fit the measured data. Two parameters that have not been set and can be used as fitting parameters are the lifetime in the germanium and the surface recombination velocities. The maximum value of the lifetime is set by the choice of starting material and implanted contact design. Lifetime can be lowered significantly by the fabrication process. This is especially true in the implanted emitter region where damage from the implant process is inadequately removed. The surface recombination velocities are set by the device design and the passivation techniques used. One of the best indicators of the magnitude of the surface recombination velocity for non-ohmic surfaces is the internal quantum efficiency measurement at short wavelengths.

It is possible to separate the results of the internal quantum efficiency measurements into wavelength regions that are dominated by one region only in the device. At short wavelengths, the majority of the generation is in the emitter region because of the large absorption coefficients. As the wavelength of the illumination is increased, the generation takes place deeper into the device until the base region is
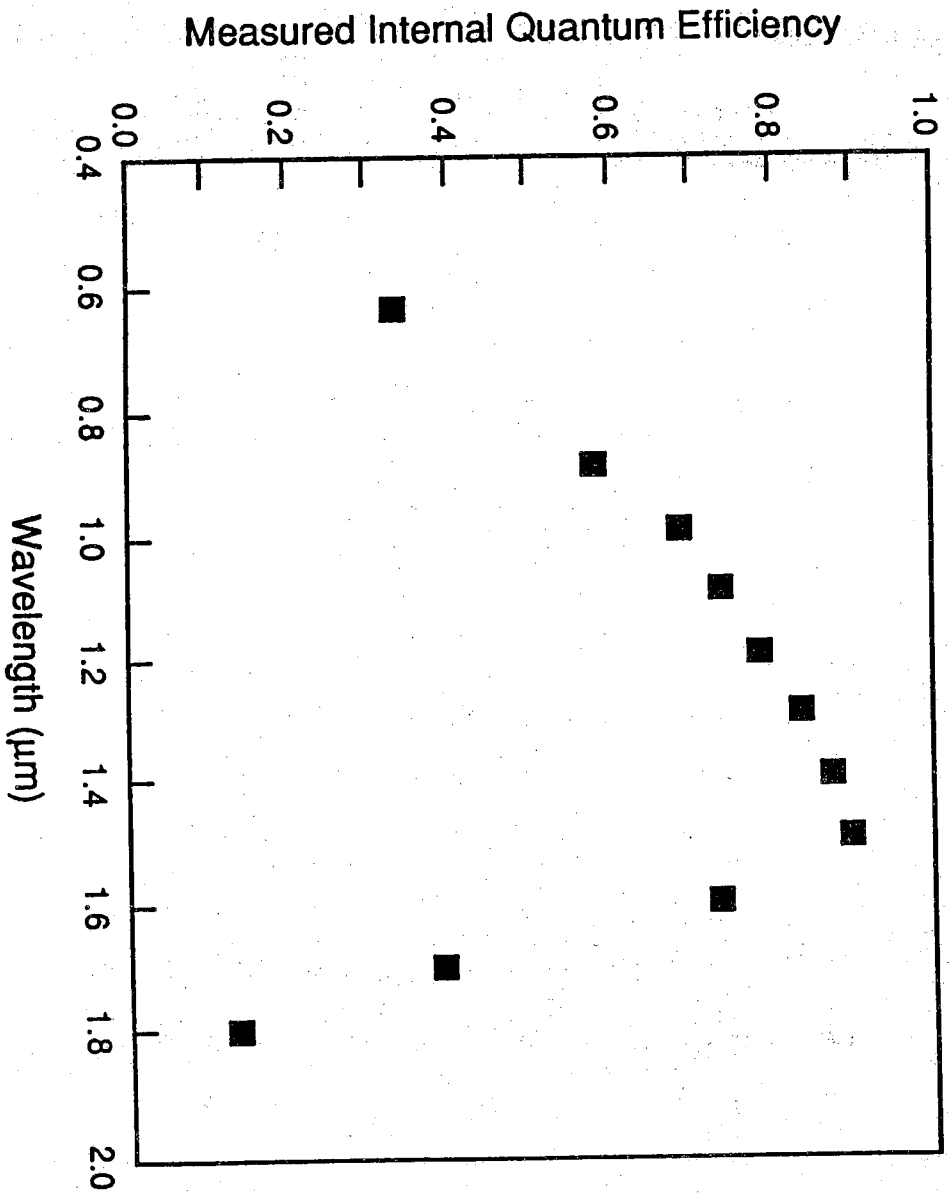
Figure 5.1
Measured Internal Quantum Efficiency

the dominate generation region. For sufficiently long wavelengths some photon flux is transmitted through the back of the device and is lost to the collection process. Therefore, it is possible to observe the effect of varying the magnitude of the emitter and base lifetimes separately in the short and long wavelength regions, respectively.

Results of the SCAP1D simulation of the corrected internal quantum efficiency are shown in Figure 5.2. This fit was obtained by adjusting the lifetime in the base and emitter regions. The lifetime is given by

$$\tau = \frac{\tau_0}{1 + N/N_{ref}} \qquad (5.3)$$

where τ_0 is the lifetime for low doping levels, N is the doping concentration, and N_{ref} is the breakpoint used to set the effect of doping on the lifetime. The magnitude of N_{ref} was $1 \times 10^{15} cm^{-3}$ for all simulation runs. In the base region a τ_0 of one millisecond was used. For this device with a base doping of $2.3 \times 10^{17} cm^{-3}$ the base lifetime was approximately five microseconds.

The lifetime in the emitter region is lowered due to an incomplete removal of implant related damage by thermal annealing. In the implanted layer the damage profile has roughly the same shape as the implant profile. Since the exact shape of the damage profile for the fabricated devices was not known, the effect on the emitter lifetime was modeled as a region of constant τ_0 of .5 microseconds that extends from the semiconductor surface to the edge of the space-charge region at .23 microns. The lifetime in the space-charge region was determined by fits to the forward current-voltage characteristics and will be discussed below. Because of the operating conditions for the experiment and the small width of the space-charge region compared to the device width, the internal quantum efficiency is not greatly affected by recombination in this region.

The recombination velocities at the front and back surfaces also need to be set in the model. The back surface recombination velocity is set to a large value since this surface is an ohmic contact. The choice of value for the front surface recombination velocity is tied to the lifetime used in the emitter. Because of the narrow emitter and the extremely low lifetime in it, the front surface recombination velocity can be set to zero without appreciably changing the simulation results. As the emitter damage is removed, increasing the lifetime, the front surface recombination velocity will have to be set more accurately.

Justification for the assertion that the emitter and base region lifetimes could be chosen separately by observing the response at the short and long wavelengths can be seen in plots of the recombination as a function of position in the device. Figure 5.3 shows the integrated recombination rate as a function of wavelength for the emitter and base regions and the recombination due to the ohmic contact at the back of the device.

For long wavelengths, the quantum efficiency simulation results are lower than the measured data (Fig. 5.2). This can be attributed to inaccuracies in the calculation of η_{meas} due to the finite spectral width of the optical system used in the measurement. Because of the finite bandwidth of the illumination source the incident spectrum is not truly monochromatic and the resulting internal quantum efficiency is actually an average over a band of wavelengths. In regions where the absorption coefficient is slowly varying, the error in the measurement is negligible. But, at wavelengths at or near the absorption edge of germanium where the absorption coefficient is rapidly changing this finite bandwidth leads to an over estimate of the
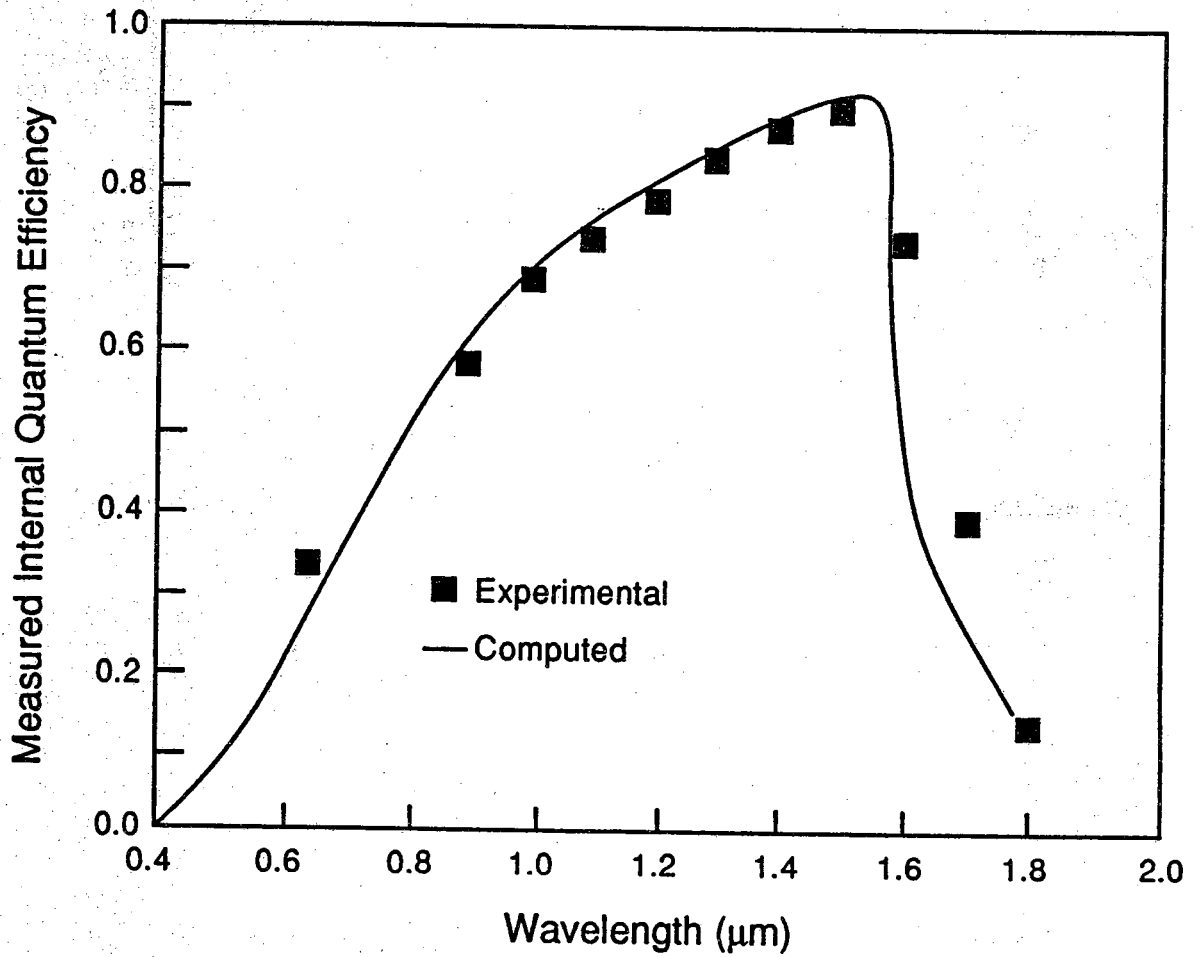
Figure 5.2
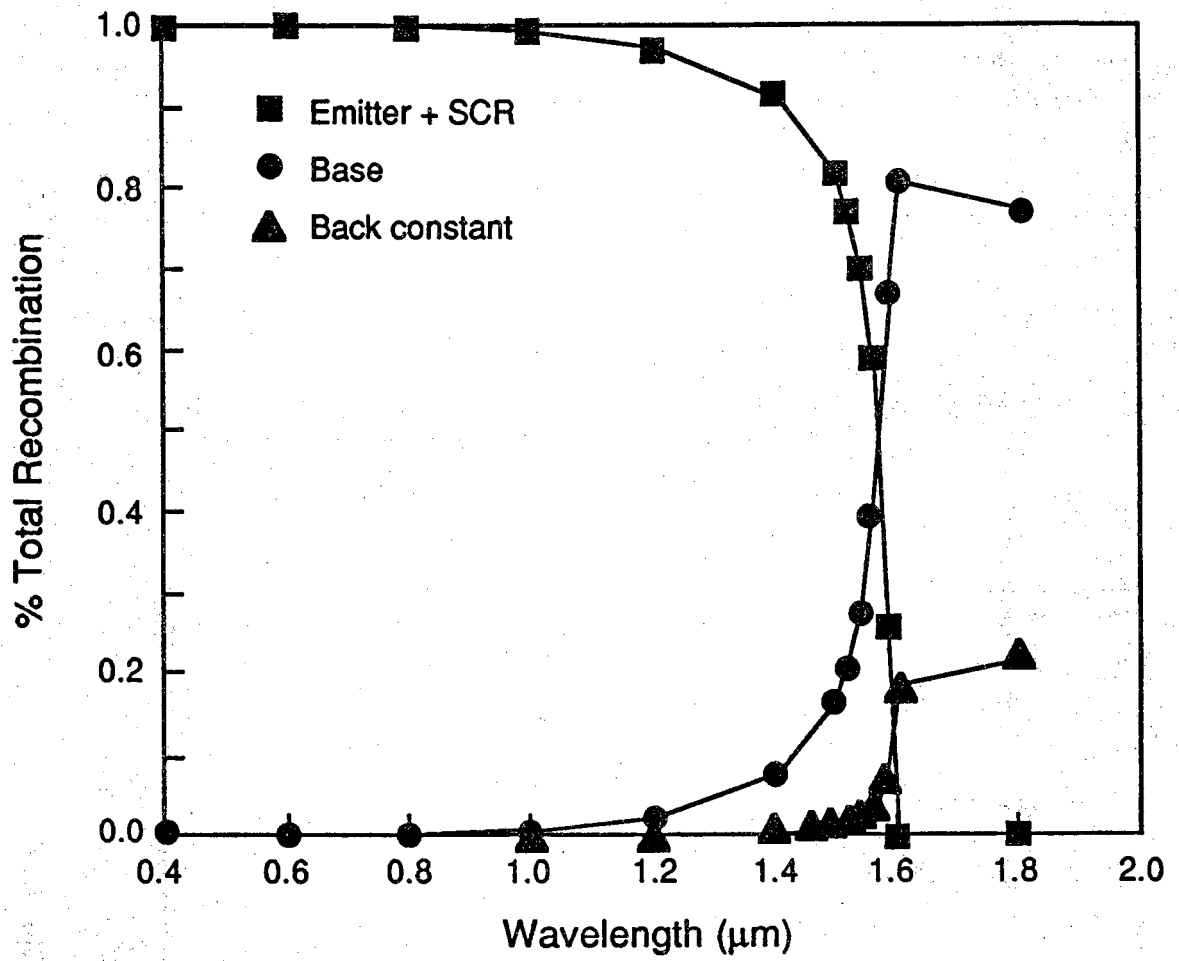A Comparison of the Measured and Computed Internal Quantum Efficiency.

Figure 5.3
Integrated Recombination Rate

response.

The absorption edge region is also very sensitive to temperature and doping concentration. Errors in recording the actual device temperature during the measurement, coupled with inaccuracies of the computer model for absorption coefficient, make simulation of the measured data difficult.

The simulation results are also lower than the experimental values in the short wavelength region. This is probably a result of setting the effect of the implant damage to the lifetime to be constant over the entire emitter region. Since the shape of the damage region is not known, further refinement of the lifetime in this region would be speculative at best.

5.5 Forward Bias Simulations

While the analysis of the internal quantum efficiencies lead to an estimate of the emitter and base lifetimes for the measured device, analysis of the forward bias current-voltage characteristics are needed to determine the lifetime in the space-charge region. Equation 5.5 gives the ideal diode equation for a diode that has major contributions to the forward current from both the quasi-neutral emitter and base regions and the space-charge region.

$$I_D = I_{o_1} (e^{\frac{qV_D}{k_B T}} - 1) + I_{o_2} (e^{\frac{qV_D}{2k_B T}} - 1) \qquad (5.4)$$

The terms I_{o_1} and I_{o_2} are the ideal saturation currents derived for the quasi-neutral and space-charge regions, respectively. For a one-sided, n^+-p step junction, I_{o_1} is given by

$$I_{o_1} = qA \sqrt{\frac{k_B T \, \mu_n}{q\tau_n} \frac{n_i^2}{N_A}}$$

The I_{o_2} term can be approximated with the expression

$$I_{o_2} \approx 1/2 qA \frac{n_i}{\tau_{SCR}} W \qquad (5.5)$$

the variables used retain their usual definitions. This expression assumes that the recombination rate is constant throughout the space-charge region. Evaluation of I_{o_2} is hampered due to the fact that W, the space-charge region width, is a strong function of the applied bias and the doping profile of the device.

If series resistance effects are included, Equation 5.5 must be modified by replacing V_D with $(V_{app} - I_D R_S)$, where V_{app} is the applied bias. Then

$$I_D = I_{o_1} (e^{\frac{q(V_{app} - I_D R_{S_D})}{k_B T}} - 1) + I_{o_2} (e^{\frac{q(V_{app} - I_D R_{S_D})}{2k_B T}} - 1) \qquad (5.6)$$

The amount of series resistance in the device can be estimated by examining the high current portion of the dark I-V characteristic as in Figure 5.4. If it is assumed that,
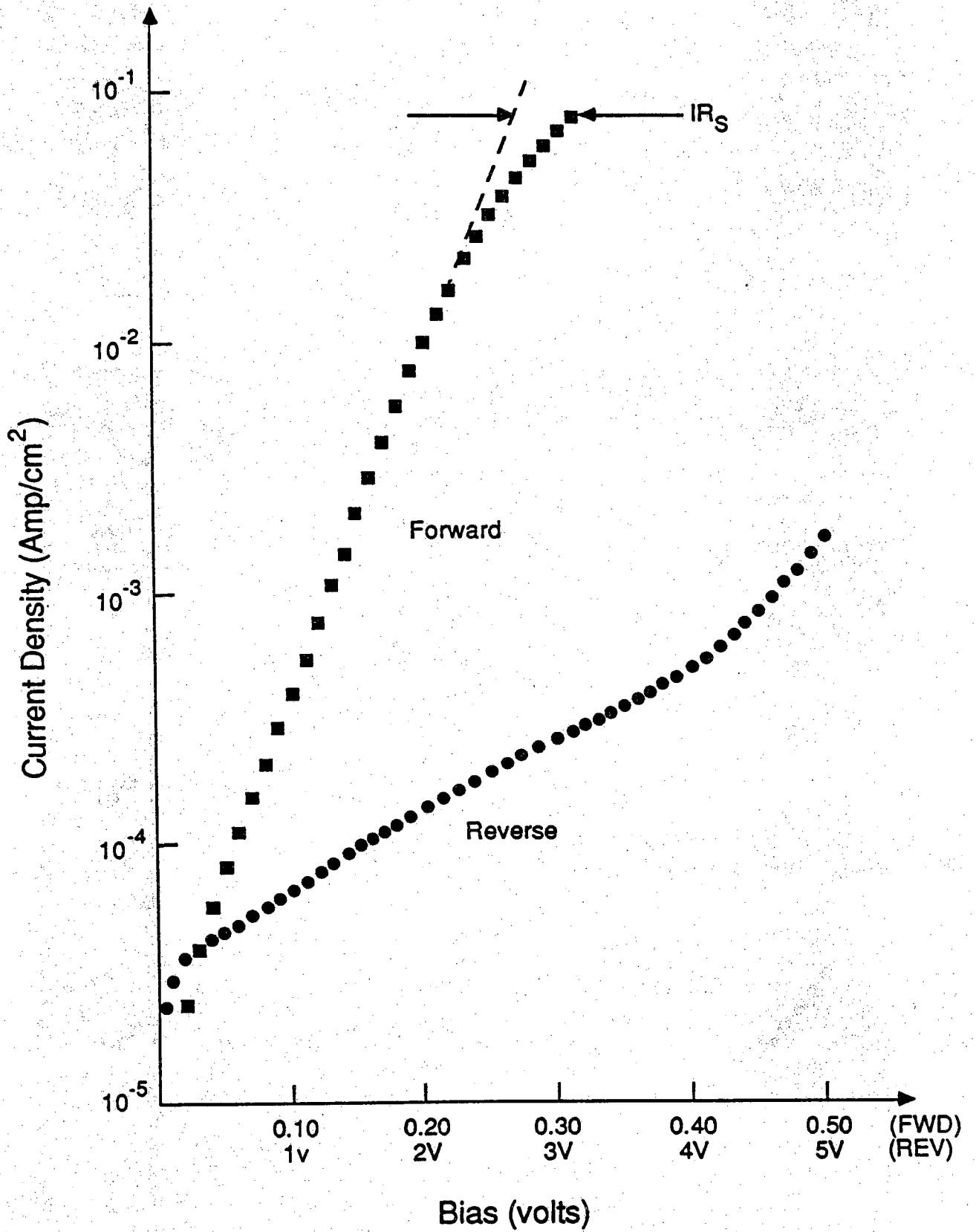
Figure 5.4
Dark J-V

for large currents, the dark current, I_D is dominated by the I_{o_1} term, Equation 5.9 can be used to determine the series resistance by using the measured data at two values of applied voltage in this range.

$$R_S = \frac{V_h - V_l - \dfrac{k_B T}{q} \ln \left| \dfrac{I_h}{I_l} \right|}{I_h - I_l} \tag{5.7}$$

where the subscripts refer to the higher and lower measured values. Evaluation of this expression for the data shown yields a series resistance value of $\simeq .7\Omega$. However, the value obtained is not constant with voltage even at large biases, and therefore it can not be used to reliably correct the measured data for series resistance effects. The non-constant series resistance is thought to be an indication of the two-dimensionality of the device as it is forward biased and would not be predicted by the simple theory presented above.

In order to obtain a model for the device operation in forward bias without the difficulty of removing the series resistance effect from the data, measurement of the current-voltage characteristics under illumination was made. This analysis uses the shifting approximation and is valid as long as the principle of superposition holds for the device and measurement. If superposition is valid, then the expression for current in an illuminated device is given by the dark current (Equation 5.4) shifted by the current generated due to the illumination, I_L:

$$I = I_D - I_L \tag{5.8}$$

Under illumination, the bias at which the diode current is equal to zero is defined as the open-circuit voltage, V_{OC}, and the short-circuit current, I_{SC}, is defined as the current measured at a bias of zero volts. If there is no series resistance in the device, a measurement of I_{SC} versus V_{OC} under illumination will be equivalent to a measurement of I_D versus V in the dark. The superposition principle allows a one-to-one correspondence to be made between a $I_{SC} - V_{OC}$ and $I_D - V$ pairs of data. If the illuminated I-V curve is slowly changing in current near zero bias, then the error in taking I_{SC} to be equal to I_L will be small and the $V_{OC} - I_{SC}$ measurement can be used as a valid approximation to the measurement of I_D with the series resistance removed from the experiment. Examination of the zero bias region of the diode characteristic indicates that the above approximation is valid for this device.

The results of measuring V_{OC} and J_{SC} while varying the incident intensity is plotted in Figure 5.5. A least-square's fit of the data to Equation 5.4 yield values for the two saturation current densities given in Table 5.2.

Table 5.2

$J_{o1} = 11.9\,\mu A/cm^2$
$J_{o2} = 34\,\mu A/cm^2$

SCAP1D was used to simulate the dark I-V measurement using the device model developed above for the internal quantum efficiency simulation. The computed results are shown in Figure 5.6. The dashed lines in the figure were obtained by fitting the SCAP1D results to Equation 5.4 and are the components of the current attributed to
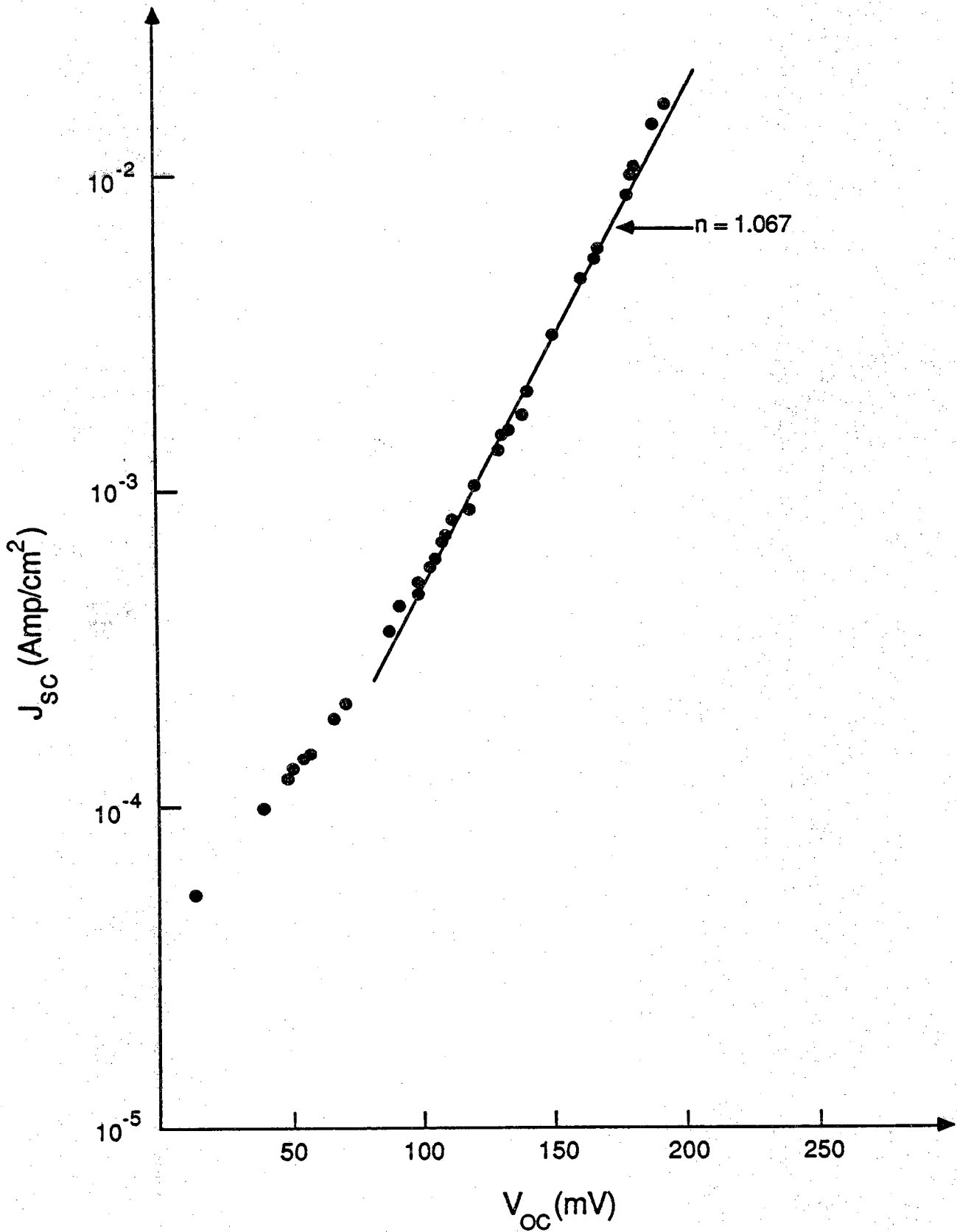
Figure 5.5
J_{sc} vs V_{oc} for the Diode of Figure 5.4.

each region as above as determined by SCAP1D. For the purposes of this computation, the width of the space-charge region was obtained from the extent of the region of non-zero electric field at low bias as calculated by SCAP1D. The space-charge region was computed to extend from $.23\mu$m to $.345\mu$m in the device.

5.6 Conclusions

As a result of the relatively good agreement between simulation and experiment, it is felt that the device was well characterized and that the model can be used to optimize the cell designs and predict the TPV performance of future germanium cells. This will be discussed in Chapter 6.

5.7 References

1. G. D. Mahan, Phys. Rev. B, vol. 5, p. 594, 1972.
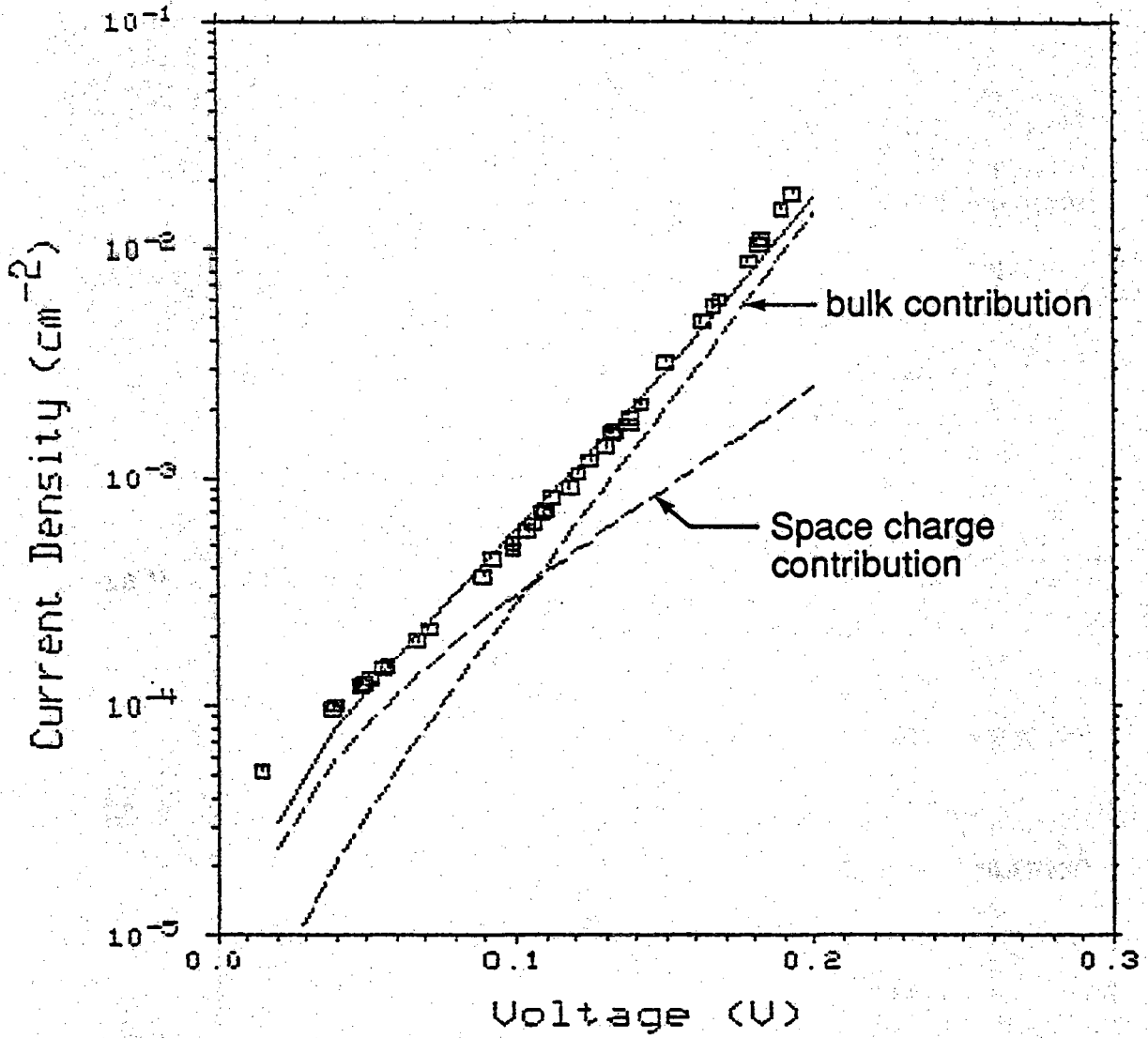
Figure 5.6

A comparison between measured and computed J-V characteristics. The dashed lines are contributions from the space change region and the bulk of the diode.

CHAPTER 6

CELL PROJECTIONS

6.1 Introduction

In this chapter we will use the results of the computer fit to the experimental data to examine the performance of germanium thermophotovoltaic cells under various operating conditions and assumptions. We will begin by examining the performance of this cell as is. That is, we will take the device which was measured and characterized in previous chapters and examine its performance when illuminated with various spectra. The spectra to be examined include blackbody spectra at 1500 and 1700 °K, an AM1.5 spectrum at a concentration of 100 after passing through a 200 micron thick silicon filter, and the spectra of an Er_2O_3 emitter operating at 1400, 1600, 1800 and 2000 °K. We will then examine the factors which limit the performance of the cell and ask the question, "What will happen to the performance of the cell if we remove the barriers to performance one at a time?" This will lead us to an optimized cell design based on realistic assumptions for what one could eventually expect to be able to do with a germanium device. We will then examine the limitations imposed upon an optimized device and discuss possible techniques for further reducing the losses and increasing the performance. Finally, we will discuss the operation of an idealized optimized germanium cell when a selective reflector is placed between the illumination source and cell.

6.2 "As is" Cell Performance

Table 6.1 lists the critical parameters for the "as is germanium cell." These are the parameters which are appropriate to the measured values presented in Chapters 4 and 5 and are the values which were obtained through careful fitting of the SCAP1D simulation and experiment. In all cases, we have assumed that bandgap narrowing is occurring according to Mahan's model, Auger recombination is present, and free carrier absorption of the illumination is also taken into account.

In Table 6.2 we show the open circuit voltage, V_{oc}, short circuit current, J_{sc}, fill factor, FF, collection efficiency, η_{coll}, and operating efficiency, η, for each of these spectra.

We find that the conversion efficiency of the "as is" device ranges from about 4% for a 1500 °K blackbody source to 9.1% for a 2000 °K Er_2O_3 source. Certainly not a very high value and certainly not one of much practical interest. Careful examination of the simulations indicates that the primary problem is with the open circuit voltage. Open circuit voltage only reaches a value of .369 volts, which is just over half of the bandgap. When we examine the reason for the limitation on the open circuit voltage, we find that recombination in the emitter dominates the performance of the cell. The emitter lifetime in the "as is" device is extremely low. We believe incomplete annealing of the ion implant damage causes the very low emitter lifetime.

Table 6.1
"As is" Cell Parameters

Parameter	Value
Device Thickness	280 μm
Auger Recombination	True
Back Contact	Ohmic
Front Surface Recombination Velocity	0.0 cm/sec
Emitter Doping Shape	Gaussian
Emitter Junction Depth	.28 μm
Back Surface Field Junction	.26 μm
Emitter Peak Doping	2.86×10^{20} cm^{-3}
BSF Peak Doping	3×10^{20} cm^{-3}
τ_o (emitter)	0.5 μs
τ_o (space charge region)	13 μs
τ_o Base	1 ms
Base Doping	2.29×10^{17} cm^{-3}
Band Gap Narrowing	Mahan
Free Carrier Absorption	True
Back Surface Reflection	.63
Cell Temperature	22 $^\circ$ C

Table 6.2
"As is" Cell Performance

Spectrum	Intensity (W/cm^2)	J_{sc} (A/cm^2)	V_{oc} (Volts)	FF	η_{coll} %	η %
1500 $^\circ$ K Blackbody	28.7	4.51	0.3498	0.7396	73.22	4.06
1700 $^\circ$ K Blackbody	47.3	10.27	0.3706	0.7399	74.17	5.95
100$\times$AM1.5$\rightarrow$200μmSi	8.31	2.45	0.3342	0.7347	48.91	7.22
1400 $^\circ$ K Er$_2$O$_3$	3.99	0.65	0.3001	0.7671	76.71	3.52
1600 $^\circ$ K Er$_2$O$_3$	7.88	1.78	0.3260	0.713	76.09	5.39
1800 $^\circ$ K Er$_2$O$_3$	15.88	4.32	0.3487	0.7394	76.13	7.02
2000 $^\circ$ K Er$_2$O$_3$	29.47	5.80	0.3694	0.7399	75.45	9.09

6.3 Improved Emitter Device

Since there are a number of experimental techniques for removal of implantation damage, it would seem that one might reasonably expect to be able to significantly reduce the residual damage and consequently increase the lifetime in the emitter. Under the assumption that this can be accomplished, we have examined the performance of the germanium cell with an undamaged emitter. We have assumed that τ_0 can be as large as 1×10^{-3} sec. Recall that τ_0 is the lifetime in the absence of any doping relating reductions in lifetime. In fact when doping related reductions in lifetime are included, this results in an emitter lifetime in the vicinity of 10 nsec near the doping maximum. It is a reasonable expectation that this value can be reached or even exceeded. Table 6.3 presents the results of simulations of this "improved emitter" device. We observe that all parameters J_{sc}, V_{oc}, F.F., and η are improved as a result of improvements in the emitter. We now observe that the conversion efficiency has risen to 5% for a 1500 °K blackbody source and 11.5% for a 2000 °K Er_2O_3 source. We now find that the device is dominated by recombination in the base. Therefore the next device to be examined is one in which the base lifetime is increased.

One way to increase the base lifetime is to reduce the base doping from the "as is" value of 2.3×10^{17} to a somewhat lower value. We have examined two cases, base doping of $1 \times 10^{15} cm^{-3}$ and $1 \times 10^{16} cm^{-3}$. The results of calculations using these doping densities with no other changes in the devices are shown in Table 6.4. The performance of the device is improved with the collection efficiency rising to a value of .97. Thus, nearly every hole-electron pair generated is collected and the primary limitation on performance is again the open circuit voltage. The conversion efficiency is observed to rise from the previous value of 5.03% to 6.28% for the $1 \times 10^{16} cm^{-3}$ base doping and 6.61% for the $1 \times 10^{15} cm^3$ doping. Under the operating conditions examined here, the base has entered high injection. The result is that the back surface field is not effective in keeping minority carriers away from the high recombination back contact. This is true for both base dopings, and, as a matter of fact, the recombination is now dominated by the back contact. The next step in improving the device is clearly to attempt to make a more effective back surface field region.

6.4 Improved Back Surface Field

Since the doping level in the back surface field region is already quite high, one way to improve the effect of the high low junction is to make the junction much deeper. In the "as is" device, the back surface junction was 0.26 μm deep. For purposes of the next calculation, this has been increased to 2 μm. This depth would require a high temperature diffusion for a long time and probably represents the practical limit of back surface field junction depth. It also increases the risk of significantly reducing the lifetime because of the high temperature and long diffusion times.

Table 6.5 shows the effect of increasing the back surface field junction depth. In the case of the $1 \times 10^{16} cm^{-3}$ base doping the short circuit current is decreased, the open circuit voltage increased, the fill factor decreased and the overall conversion efficiency decreased. In the case of the more lightly doped base ($1 \times 10^{15} cm^{-3}$) the short circuit current is decreased, the open circuit voltage is increased, the fill factor

Table 6.3 "Improved Emitter" Cell Performance
(assume a minimum emitter lifetime of 10 ns)

Spectrum	Intensity (W/cm^2)	J_{sc} (A/cm^2)	V_{oc} (Volts)	FF	η_{coll} %	η %
1500 °K Blackbody	28.7	4.91	0.3869	0.7598	79.73	5.03
1700 °K Blackbody	47.3	11.35	0.4061	0.7598	82.00	7.43
100×AM1.5→200μmSi	8.31	1.42	0.3556	0.7513	85.62	4.57
1400 °K Er$_2$O$_3$	3.99	0.69	0.3372	0.7434	81.29	4.34
1600 °K Er$_2$O$_3$	7.88	1.92	0.3631	0.7539	81.91	6.66
1800 °K Er$_2$O$_3$	15.88	4.74	0.3861	0.7596	83.56	9.76
2000 °K Er$_2$O$_3$	29.47	11.00	0.4072	0.7598	84.67	11.53

Table 6.4
Reduced Base Doping Cell

Base Doping (cm^{-3})	Spectrum (W/cm^2)	J_{sc} (A/cm^2)	V_{oc} (Volts)	FF	η_{coll} %	η %
1×10^{16}	1500 °K Blackbody	6.38	0.3934	0.7172	97.47	6.28
1×10^{15}	1500 °K Blackbody	6.47	0.3956	0.7145	98.23	6.61

Table 6.5
Increased Back Surface Field Depth (2.0μm)

Base Doping (cm^{-3})	Spectrum (W/cm^2)	J_{sc} (A/cm^2)	V_{oc} (Volts)	FF	η_{coll} %	η %
1×10^{16}	1500 °K Blackbody	6.10	0.4084	0.7128	97.56	6.19
1×10^{15}	1500 °K Blackbody	6.18	0.4149	0.7465	98.15	6.67

is increased and the conversion efficiency is increased.

An examination of the recombination shows that while a deep back surface field is better than a shallow one, it does not work as well as one might expect, due to the high injection conditions in the base. However, it has worked well enough that the emitter is once again limiting V_{oc}. If we examine the details of the recombination which occurs in the emitter, we find that it is now dominated by Auger recombination. There is also some effect from bandgap narrowing in both the emitter and the back surface field. The next step is to examine techniques for reducing the emitter recombination through further device design changes.

6.5 Reduced Emitter Doping

There are a number of ways to reduce the recombination in the emitter. One would be to make the emitter much thinner. However, this has the disadvantage that as the sheet resistance of emitter rises, it can cause serious problems due to an increase in series resistance. Another approach would be to reduce the peak value of the doping from the original value of 2×10^{20} cm^{-3}. We have chosen to examine two cases, 2×10^{19} cm^{-3} and 5×10^{18} cm^{-3}. Reductions much below this lead to serious problems with sheet resistance and are not deemed practical. The results of these changes are shown in Table 6.6. The device performance improves about 10% by reducing the doping to 2×10^{19} cm^{-3}. Very little further improvement occurs through reducing the doping to 5×10^{18} cm^{-3}. Collection efficiency is improved to nearly 99% in this case. We have succeeded in reducing the emitter recombination to the point where once again the back surface field region dominates the recombination under open circuit conditions. Since there is no simple way to further reduce the recombination in the back surface field region, the next attempt was to examine the effects of changing the thickness of the base region to see if a more optimum base thickness could be reached.

6.6 Optimized Base Width

Increasing the base width might be expected to increase the absorption of photons, and hence, increase the short circuit current. On the other hand, if the diffusion length is shorter than the base width, this can lead to increased recombination and a decrease in device performance. Two cases were examined, the base width was changed from the previous value of 280 microns to 100 microns, for a thin device, and 400 microns for a thick device. The results of these calculations are shown in Table 6.7. The thin device (100 microns) performance decreases as compared to the 280 micron device while increasing the thickness to 400 microns increases device performance. In both cases the lightly doped base, is about 10% better than the more heavily doped base. Again, we find that the recombination at open circuit is dominated by the back surface field region. Recombination in the emitter is primarily due to Auger effects and the base is still in high level injection, thus reducing the effectiveness of the back surface field. Table 6.8 shows the predicted performance of the optimized cell under a variety of spectra.

Further improvements in device performance are thought to require major design changes. Since the primary problem is the lack of effectiveness of the back surface field region, it is felt that further improvements will require one or more of the

following.

1) Development of a heterojunction contact which allows easy passage of majority carriers while blocking minority carriers;

2) A significant reduction in the effective recombination at the back metal semiconductor contact. This might be obtained by reducing the contact area or by significantly reducing the high-low junction area.

6.7 Effects of Front Surface Recombination

Throughout the previous calculations, we have assumed that the front surface is carefully passivated. While it is relatively easy to fabricate passivated surfaces for low injection conditions, under high illumination conditions, surface passivation sometimes becomes much less effective. To examine the effect of a loss of surface passivation, we have performed a series of runs in which the surface recombination velocity was increased from 0 to 10^4 cm/sec. The results are presented in Table 6.9. There is nearly a 10% degradation in conversion efficiency if the front surface is not carefully passivated. One will have to take precautions to make sure that the surface is carefully passivated in an optimized cell.

6.8 The Effect of a Selective Reflector

One of the attractive features of a thermophotovoltaic system is that it allows one to control the spectrum which falls upon the thermophotovoltaic cell. It's been proposed that one can develop selective reflectors which will pass only those wavelengths which are most efficiently converted by the cell and return the energy at long and short wave lengths to the source. In order to examine the performance of the system with an idealized selective reflector a series of runs were made in which it was assumed that only energy within a given bandwidth below 1.6 microns would be transmitted to the cell. The conversion efficiency was then defined as the electrical output divided by the energy incident on the cell. A series of filter bandwidths from 0.1 to 1.5 microns. were examined. The results are presented in Table 6.10. It can be seen that a very high conversion efficiency is available if these idealized bandwidths can be approached, the efficiencies range from 34 to 38%, certainly very attractive conversion efficiencies.

6.9 Recommendations for Future Work

There are a number of areas in which future work should be concentrated.

Recombination in the emitter will need to be minimized if ion implantation techniques are used for fabrication of the emitter. This means that effective techniques for removing implant damage will need to be developed. One of the reasons that ion implantation is desirable is that it is easy to perform on germanium. Diffusion techniques are not well developed in germanium, although the need for high quality emitters may force future devices to use diffusion technology. It appears that the

Table 6.6
Reduced Emitter Doping

Peak Emitter Doping (cm^{-3})	Spectrum (W/cm^2)	J_{sc} (A/cm^2)	V_{oc} (Volts)	FF	η_{coll} %	η %
2×10^{19}	1500° Blackbody	6.03	0.4221	0.7218	99.40	6.69
2×10^{19}	1500° Blackbody	6.36	0.4290	0.7684	99.82	7.30
5×10^{18}	1500° Blackbody	6.30	0.4226	0.7220	99.41	6.70
5×10^{18}	1500° Blackbody	6.36	0.4295	0.7691	99.83	7.32

Table 6.7
Effects of Thick (100μm) and Thin (400μm) Base Widths

Base Width (μm)	Base Doping (cm^{-3})	Spectrum (W/cm^2)	J_{sc} (A/cm^2)	V_{oc} (Volts)	FF	η_{coll} %	η %
100	1×10^{16}	1500°K Blackbody	5.26	0.4236	0.7588	99.79	5.89
400	1×10^{16}	1500°K Blackbody	6.68	0.4197	0.6965	99.12	6.81
100	1×10^{15}	1500°K Blackbody	5.28	0.4261	0.7771	99.92	6.09
400	1×10^{15}	1500°K Blackbody	6.75	0.4292	0.7623	99.56	7.70

Table 6.8
Optimize Cell Performance Base Thickness 400μm

Spectrum	Intensity (W/cm^2)	J_{sc} (A/cm^2)	V_{oc} (Volts)	FF	η_{coll} %	η %
1500°K Blackbody	28.7	6.75	0.4292	0.7623	99.56	7.70
1700°K Blackbody	47.3	14.96	0.4489	0.7713	99.28	10.95
100×AM1.5→200μmSi	8.31	1.76	0.3939	0.7379	99.90	6.14
1400°K Er$_2$O$_3$	3.99	0.92	0.3760	0.7225	99.89	6.27
1600°K Er$_2$O$_3$	7.88	2.53	0.4037	0.7453	99.83	9.64
1800°K Er$_2$O$_3$	15.88	6.07	0.4266	0.7614	99.56	12.41
2000°K Er$_2$O$_3$	29.47	13.74	0.4470	0.7712	99.28	16.07

Table 6.9
Effect of Front Surface Recombination
$(S_F = 10^4 cm/sec)$

Front Surface Recombination Velocity cm/s	Spectrum	Intensity (W/cm^2)	J_{sc} (A/cm^2)	V_{oc} (Volts)	FF	η_{coll} %	η %
0	1500° K Blackbody	28.7	6.75	0.4292	0.7623	99.56	7.70
10^4	1500° K Blackbody	47.3	6.68	0.4121	0.7253	98.46	6.95

Table 6.10
Cell Performance When Operated in Conjunction with an
Ideal Bandpass Optical Filter. Upper Cutoff ($\lambda = 1.6\mu$m)

Bandpass Width (μm)	Intensity on Cell (W/cm^2)	J_{sc} (A/cm^2)	V_{oc} (Volts)	FF	η_{coll} %	η %
0.1	1.87	2.33	0.4016	0.7444	99.84	37.23
0.2	3.66	4.40	0.4186	0.7573	99.62	38.11
0.3	5.08	5.94	0.4763	0.7624	99.51	37.98
0.4	6.56	7.42	0.4320	0.7657	99.43	37.40
0.5	7.64	8.41	0.4351	0.7674	99.38	36.76
1.5	10.00	10.22	0.4400	0.7697	99.30	34.62

base doping should be kept to 1×10^{15} cm^{-3} or less even though this does lead to high injection operating conditions in the base of the device. These high injection conditions, in turn, lead to problems of inadequate back surface field carrier containment. It appears that conventional back surface fields are not adequate and that work will need to be done to find ways to reduce recombination at the back contact or in the back surface field region. Suggested areas for future work are the development of heterojunction contacts, point contact type structures or, reduced area for the metal semiconductor contacts with well passivated surfaces in between.

An area which is absolutely critical is the development of a front surface selective reflector for these devices. It has also been proposed that one could allow the long wavelength radiation to pass through the device, be reflected off the back surface, back through the device to the source. One of the problems with this is that our calculations show that free carrier absorption is a problem; it does not appear likely that using the back surface as a reflector to return the energy to the emitting source is feasible. It is recommended that future work in this area concentrate on developing high quality selective reflectors which can be placed between the energy source and the cell. This will have the added advantage that the heat load on the cell will be significantly reduced.

6.10 Conclusions

It appears that it is technologically feasible to design a germanium TPV cell with conversion efficiencies in the range of 10% when operated with a 1700 °K blackbody source. or when illuminated by the radiation from an Er_2O_3 radiator. However, if a selective reflector with very high reflection outside the passband and very high transmission in the passband can be developed, it appears that conversion efficiencies in the in excess of 30% are feasible. Note that all of these calculations were performed assuming that the germanium cell could be maintained at a temperature of 22 °C. In some applications, that may present significant systems problem. Increases in cell temperature are particularly detrimental for germanium cells as their performance is much more temperature sensitive than that of silicon or gallium arsenide cells.